

# Chemical Functionalization of Graphene

Der Naturwissenschaftlichen Fakultät der  
Friedrich-Alexander-Universität Erlangen-Nürnberg

zur Erlangung des Doktorgrades Dr. rer. nat.

vorgelegt von

**Wei Zhao**

aus Anhui, China



Als Dissertation genehmigt

durch die Naturwissenschaftliche Fakultät

der Friedrich-Alexander Universität Erlangen-Nürnberg

Tag der mündlichen Prüfung: 07.11.2013

Vorsitzender der Promotionskommission: Prof. Dr. Johannes Barth

Erstberichterstatter: Prof. Dr. Hans-Peter Steinrück

Zweitberichterstatter: Prof. Dr. Andreas Görling



## Contents

1.	Introduction .....	1
2.	Fundamentals and Methods .....	10
	2.1 X-ray Photoelectron Spectroscopy (XPS).....	10
	2.2 Synchrotron radiation.....	12
	2.3 The “synchrotron machine” .....	14
	2.4 TPD and TPXPS .....	16
	2.5 Low Energy Electron Diffraction (LEED).....	18
3.	Results .....	19
	3.1 Adsorption structure of graphene on Ni(111) [P1] .....	19
	3.2 N-doped graphene by N ion bombardment [P2] .....	23
	3.3 N-doped graphene by CVD of pyridine [P3] .....	26
	3.4 B-doped graphene on Ni(111) [P4, P5].....	29
	3.5 Hydrogenation of graphene [P6].....	33
4.	Summary .....	37
5.	Zusammenfassung .....	40
6.	Acknowledgement .....	43
7.	Literature.....	44
8.	Appendix: P1 – P6 .....	50



# 1. Introduction

Graphene is a single layer two-dimensional  $sp^2$  bonded carbon honeycomb network (Figure 1.1). Since free-standing graphene was unexpectedly found by Novoselov et al. in the year of 2004,<sup>1</sup> it has led to an explosion of experimental and theoretical work. Scientists have paid tremendous attention and efforts to the research of this magic material all over the world. The Nobel Prize in Physics in 2010 was awarded to A. K. Geim and K. S. Novoselov “for groundbreaking experiments regarding the two-dimensional material graphene.”

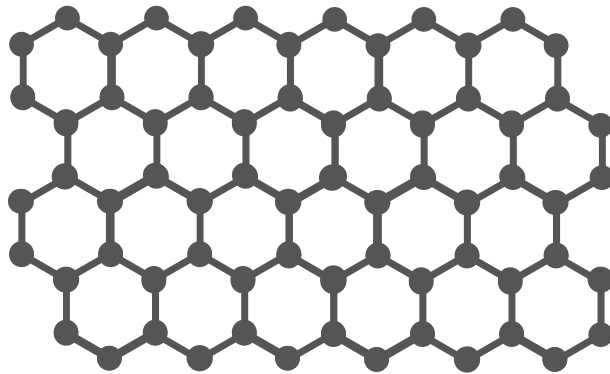


*Figure 1.1 Illustration of graphene structure.*

Graphene is a 2D material with a crystalline structure. Structurally, graphene is the basic building brick for all the other graphitic materials, i.e. it can be wrapped up into 0D fullerenes, rolled up into 1D carbon nanotubes and stacked into 3D graphite. However, for a long time, a strict 2D crystal was presumed to not exist in a free state, because it is unstable from thermodynamics, i.e. the long distance periodicity in the 2D crystal are destroyed by thermal fluctuations in the lattice, resulting in decomposition or clustering of the 2D lattice. Actually, in the early 1900s, the structure of graphite was characterized by X-ray crystallography and graphene was known as one of the single layers embedded in the stack. But, graphene was not isolated into individual planes then, and little interest was shown to graphene until Geim and Novoselov were the first to obtain free-standing graphene layers by mechanical exfoliation of small pieces of highly oriented pyrolytic graphite.<sup>1</sup> Only after experiments that suggested that the carrier charges (electrons and

holes) near the Fermi level in graphene are massless Dirac fermions,<sup>2, 3</sup> hundreds of scientists have entered this research area, resulting in a fast development in graphene related studies.

Figure 1.2 shows the band structure of free-standing graphene. The valence bands and conduction bands cross into 6 points at the Fermi level, the so-called Dirac points. Graphene shows a zero band-gap and a linear dispersion near the Fermi level. The electrons and holes show massless transport in graphene, and their behavior has to be described by a Dirac-like equation, allowing the investigation of relativistic quantum phenomena in a bench-top experiment.<sup>4</sup> The unique nature of graphene results in ballistic transport of charge carriers, i.e. the carriers can travel thousands of interatomic distances without scattering, and the mobility of carriers can be ultrahigh even up to  $\approx 100,000 \text{ cm}^2 \text{ V}^{-1} \text{ s}^{-1}$  at room temperature (300 K),<sup>5</sup> remarkably better than any material we have ever known. To this end, graphene was proposed to be one of the most promising candidates for post-silicon semiconductor material. Despite of this, many other remarkable characteristics of graphene have been discovered subsequently, such as one of the strongest materials ever tested,<sup>6</sup> novel quantum hall effect<sup>3, 7</sup> and also interesting magnetic properties.<sup>8-12</sup> Potential applications include gas sensors,<sup>13-15</sup> high temperature superconductors,<sup>16, 17</sup> solar cells,<sup>18-20</sup> supercapacitors,<sup>21-23</sup> lithium batteries,<sup>24-26</sup> and so on. Especially, the ultrahigh charge carrier mobility makes graphene promising in the application of novel ballistic electronic devices,<sup>27, 28</sup> inducing potential breakthrough in the development of super-fast computer chips.<sup>29</sup>

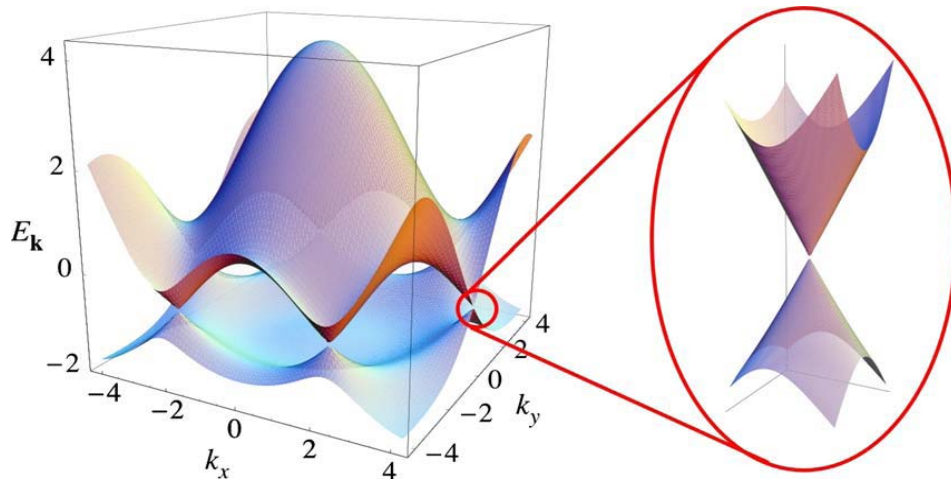


Figure 1.2 The band structure of free-standing graphene.<sup>30</sup>

To study this novel material, first of all, graphene has to be produced in proper ways. So far, there are mainly four methods to produce graphene. The first one is called micro-mechanical exfoliation of graphite. Using adhesive tape to repeatedly split graphite crystals into increasingly thinner pieces, until single or a few layers of graphene are obtained, which are then transferred onto  $\text{SiO}_2$  or Si surfaces.<sup>1</sup> However, this method does not allow for controllable production of graphene in large sizes or quantities. The second method is graphitization of silicon carbide (SiC); this is achieved by annealing SiC to high temperatures (higher than  $1100^\circ\text{C}$ ) at low pressures ( $\sim 10^{-6}$  torr) to form graphene.<sup>31-35</sup> The third one is reduction of graphene oxide by annealing in an argon/hydrogen atmosphere to yield graphene films. However, the quality of graphene produced by this way is lower due to incomplete removal of various functional groups.<sup>36-41</sup> And, the last one is epitaxial growth on metal substrates by segregation of bulk-dissolved carbon to the surface or by chemical vapor deposition (CVD) of hydrocarbons, summarized in the reviews.<sup>42, 43</sup> For segregation, carbon-containing metals are used or the metals are first doped with carbon, then annealing the metal samples at high temperatures, leads to segregation of carbon to the surface. Thereby, normally one or few layers of graphene are formed.<sup>44-47</sup> CVD is the method where an active metal surface is exposed to hydrocarbon molecules, e.g. propene, methane, or acetylene etc. at elevated temperatures,<sup>48-52</sup> so that the molecules decompose on the surface, while hydrogen desorbs, only carbon atoms are left, which arrange into a graphene layer fully covering the

surface. Conveniently, the decomposition of hydrocarbon molecules is strongly suppressed on the surface once it is fully covered by graphene, leading to a self-terminated reaction, as no active metal surface is left to facilitate the decomposition reaction. In comparison to the other methods, CVD offers a highly efficient and controllable way to synthesize single-layer graphene; the quality of graphene films, e.g. size and morphology can be tuned by altering the reaction conditions, such as pressures, temperatures and so on.<sup>42</sup> To obtain free-standing graphene, proper treatments need to be applied to remove the supporting metal.<sup>53, 54</sup>

The growth of graphene on metal surfaces is especially interesting as it could be a low energy route for its production; the growth temperatures are significantly lower compared to e.g. SiC,<sup>31</sup> and nevertheless high-quality, large-area graphene sheets can be formed.<sup>42</sup> Consequently, in recent years a lot of effort has been dedicated to the study of graphene grown on various metal surfaces.<sup>42, 51, 55-59</sup> The usually used metal substrates include copper, nickel, ruthenium, etc. Graphene grows both on single and poly crystalline metal surfaces.<sup>12, 42, 43, 59-63</sup> The CVD processes are performed at ambient conditions or in vacuum. Recently, surface science methods such as photoemission spectroscopy (PES),<sup>57, 64, 65</sup> Raman spectroscopy<sup>66-68</sup> and microscopy<sup>50, 51, 69</sup> are widely applied to investigate metal-supported graphene, and the especially interesting issues, e.g. morphology and electronic structure are heavily studied.<sup>42, 43</sup>

In most studies with surface science methods, for simplicity, a single crystal is used as substrate, because the surface of a single crystal is strictly defined and it is easy to identify the influence of the substrate on the growth of adsorbates. In addition, the adsorption sites and geometry of adsorbates on single crystals are easy to analyze, and the impact of the adsorption structure on the properties of the adsorbates is accessible. For graphene on single crystal surfaces not only the electronic structure is of interest,<sup>70</sup> but also the chemical modification of graphene sheets and their growth mechanism is in the focus of research efforts.<sup>4, 37, 71-74</sup> Among the large number of single metal crystals used as substrates for graphene growth, Ni(111) has the most similar lattice constant (2.49 Å) to that of graphene (2.46 Å); this results in a commensurate structure for

graphene grown on Ni(111).<sup>61</sup> In this thesis, a Ni(111) single crystal was used as substrate to produce pristine (or doped) graphene layers and for the subsequent studies of chemical functionalization of graphene.

The growth behavior and the structure of graphene on a Ni(111) single crystal surface was previously debated, with still contradictory results coming both from experiments<sup>55, 61, 75-77</sup> and from density-functional theory (DFT) calculations employing various approaches.<sup>78, 79</sup> All calculations agree in predicting that an almost planar carbon sheet is formed on Ni(111). However, the adsorption geometry of graphene sheet relative to the Ni(111) substrate is a matter of debate.

Since graphene was found, due to its unique properties introduced above, considerable promising applications have been expected from graphene-based materials. Attempts of producing room temperature field effect transistors from graphene have been already reported.<sup>74, 80, 81</sup> However, up to now, no straightforward way or technique for industrial production, and also applications based on graphene were shown. For example, the use of graphene in electronic applications imposes further challenges, i.e. the precise tuning of the band-gap and the charge carrier concentration. Thus, feasible approaches that manipulate the properties of graphene are strongly desired. In recent years, chemical functionalization emerged as a powerful method to tailor the properties of graphene, and the work about functionalized graphene materials with novel characteristics have always been a highlight in graphene research.<sup>82-86</sup> Chemical functionalization includes two modes: covalent and non-covalent. Covalent functionalization mainly includes hetero-atom doping, covalent attachment of small atoms or big organic molecules. Non-covalent functionalization includes  $\pi$ - $\pi$  interaction, wrapping with polymers, and adsorption of atoms or molecules on surface.<sup>84</sup> In comparison, covalent functionalization shows a higher stability against physical and chemical changes in the environment, making it favorable for the applications under ambient conditions. A perspective by Niyogi et al.<sup>83</sup> discussed covalent functionalization of the surface to produce dielectric regions on a graphene wafer, and described how surface chemistry is useful in engineering the electronic and magnetic properties of graphene. Covalent functionalization is able to

modulate the band-gap, electron scattering, and other physical properties.<sup>82</sup> Beyond electronics, covalent functionalization also shows a great importance for other application areas. For example, transparent and conductive graphene for touch panels or smart screens can be improved by covalently attaching polymers or other functional groups.<sup>82</sup> In the field of super capacitors, surface chemistry also plays an crucial role in determining the capacity and lifetime.<sup>82, 85</sup> In this thesis, one focus lies on the covalent functionalization of graphene, and the main goal is the modification of supported graphene layers by inserting hetero atoms into the graphene network. In our studies, we put particular focus on the control of the chemical and electronic properties of graphene.

In silicon semiconductor technology, the term hetero-atom doping is reserved for a controlled contamination of the material by inserting impurities in the host lattice. In the recent past, hetero-atom doping has been demonstrated a feasible and powerful method in order to tailor the electronic properties of graphene, such as shifting the valence bands.<sup>30, 87, 88</sup> The neighbors of carbon in the periodic table, boron (B) and nitrogen (N), are the natural candidates for graphene doping, due to their physical similarities, e.g., the atomic radius. Chemically, boron and nitrogen are hole and electron donors to carbon, leading to *p*- and *n*-type semiconductors, respectively, and yielding materials with great potential in graphene-based nano-scale electronic applications.<sup>74, 89-91</sup> Moreover, doping is a particularly important aspect for the purpose of adjusting the carrier concentration and type, which is a step forward towards the realization of graphene transistors<sup>74</sup> and *p*-*n* junctions.<sup>92</sup> The theoretical study indicates that the chemical properties of nitrogen-doped graphene, such as doping density and the site of the inserted nitrogen atoms, can dramatically change its physical properties, including the electronic and magnetic characteristics.<sup>93</sup> Chemically induced mobility gaps were theoretically predicted upon the incorporation of boron impurities in graphene nanoribbons (GNRs), which could open a path to better on/off ratios in GNR-based transistors.<sup>94</sup> Recently, N-doped graphene and B-doped graphene have been synthesized by a variety of methods, e.g., chemical vapor deposition (CVD),<sup>88, 95-97</sup> ion implantation,<sup>98-100</sup> electrothermal reaction,<sup>74</sup> redox reaction,<sup>26, 37, 101</sup> and arc-discharge of graphite in the presence of N- or B-containing gases.<sup>89</sup>

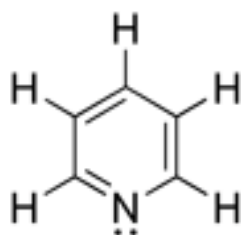
Hydrogenation is also of great importance for covalent functionalization of graphene. It was demonstrated that the reversible hydrogenation of graphene allows for controlling the electrical properties of single layer graphene.<sup>71, 102</sup> Electronically, graphene is a zero-gap semi-metal, and the fully hydrogenated graphene -graphane (CH) is an insulator with a band-gap of 3.5 eV.<sup>103</sup> The electronic properties of hydrogenated graphene are strongly affected by the hydrogen coverage and chemisorption pattern.<sup>104, 105</sup> In recent years, hydrogen storage based on graphene materials has attracted considerable attention, due to its promising performances in hydrogen storage capacity and control of storing/releasing hydrogen at proper temperatures (300 ~ 600 K).<sup>106</sup> Graphane,<sup>103</sup> shows a remarkable high hydrogen capacity of 8.6 wt%, which is close to the objectives of the US Department of Energy for hydrogen storage (9 wt% by 2015). To this end, understanding the fundamentals of the adsorption and reaction between hydrogen and graphene is crucial, not only due to the interest in hydrogen storage, but also for understanding and tuning its electronic properties.<sup>105</sup>

In this thesis, first of all, we performed a high resolution X-ray photoelectron spectroscopy (HR-XPS) investigation of graphene on Ni(111), which was accompanied by an ab initio density-functional theory study (collaboration with the group of Prof. Görling). Our results showed the coexistence of two structures on Ni(111), a bridge-top and a top-fcc structure (see Chapter 3.1), and clarified the issue of the adsorption structure of graphene on Ni(111) surface and ended the debates about this topic.

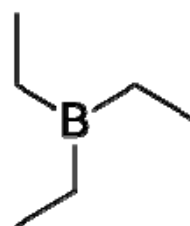
In a next step, Nitrogen- and Boron-doped graphene were synthesized on a Ni(111) surface (collaboration with the groups of Prof. Seyller and Prof. Görling).<sup>97, 98, 107</sup> First, the production of Nitrogen (N-) doped graphene will be discussed. Nitrogen-doping of graphene is a suitable route to tune the electronic structure of graphene, leading to semi-conductive materials.<sup>37, 74, 108</sup> Two methods were employed to achieve this aim, low energy nitrogen ion bombardment of graphene supported on Ni(111), and CVD growth with an N-containing precursor molecule (pyridine) on a Ni(111) surface. Both approaches appear to be simple and efficient methods towards N-doped graphene.<sup>97, 98</sup>

For preparing N-doped graphene by low energy nitrogen bombardment, a highly ordered single-layer graphene on a Ni(111) surface<sup>52, 57</sup> was exposed to a beam of low energy nitrogen ions (25 ~ 100 eV). Subsequently, we annealed the nitrogen-bombarded graphene layer to 900 K to allow for a regeneration of the perturbed graphene lattice, leading to nitrogen-doped graphene. The nitrogen-doping geometry and level are identified by in situ high resolution X-ray photoelectron spectroscopy (XPS). We also demonstrated that a nitrogen doping level of up to 0.05 monolayers (ML) is achievable and the relative amounts of nitrogen species with different doping geometries can be varied by applying different ion implantation energies and times. The details will be discussed in Chapter 3.2.

For the CVD growth of N-doped graphene on Ni(111), the precursor molecule pyridine ( $C_5H_5N$ ) was used (see Figure 1.3(a)). N-doped graphene was prepared by exposing a Ni(111) surface to pyridine at elevated temperatures leading to the formation of a single layer on the surface. By studying the C 1s and N 1s core levels, we showed that the nitrogen content can be influenced by the growth temperature, and determined the atomic structure of the nitrogen atoms as two different N-doping configurations. It was demonstrated by angle-resolved valence-band photoelectron spectra that the incorporation of nitrogen leads to a broadening of the photoemission lines and a shift of the  $\pi$ -band. DFT calculations reveal that the two N-doping configurations have different effects on the band structure, i.e. shifting the  $\pi$ -band to opposite directions. In order to decouple the N-doped graphene layer from the Ni(111) substrate, gold is used to intercalate the layer, leading to a quasi-free-standing N-doped graphene layer. The details will be discussed in Chapter 3.3.



(a)



(b)

*Figure 1.3 (a) Molecular structure of pyridine. (b) Molecular structure of TEB.*

Boron (B-) doped graphene was also produced by CVD with the precursor molecule triethylborane (TEB) (Figure 1.3(b)). This approach was shown to lead to the formation of a single layer of B-doped graphene with a high boron content (13 ~ 20%). Alternatively, annealing a boron-containing Ni(111) crystal in the presence of propene led to graphene with a lower boron content (0 ~ 5%). The boron doping configuration was identified by XPS and the impact of B-doping on the electronic structure of graphene was determined by angle-resolved valence band photoemission spectra (ARPES). In contrast to N-doped graphene, B-doping only shows the substitutional doping configuration, and the B concentration is influenced by the growth temperature. Furthermore, it is shown that the  $\pi$ -band is shifted upwards to the Fermi level by boron doping, leading to a p-type doped graphene (see Chapter 3.4). After the preparation of B-doped graphene, gold was evaporated with the intent to intercalate B-doped graphene/Ni(111). It turned out, however, that gold does not intercalate B-doped graphene for high boron concentrations (13 ~ 20%); only for lower boron concentrations (~5%) partial intercalation occurs. This result was unexpected, as gold intercalation is the well-established post treatment process for CVD-grown graphene and N-doped graphene on Ni(111) (see Chapter 3.4).<sup>10, 88, 97</sup>

As the last system presented in this thesis, hydrogenated graphene was prepared by exposing a single layer graphene supported on Ni(111) or Au/Ni(111) to atomic hydrogen. Applying XPS, the impact of hydrogenation is investigated in detail. Subsequently, also the release of hydrogen was investigated by temperature-programmed XPS and temperature programmed desorption, to elucidate the dehydrogenation process and to determine the hydrogen coverages and dehydrogenation energies. The details will be discussed in Chapter 3.5.

## 2. Fundamentals and Methods

### 2.1 X-ray Photoelectron Spectroscopy (XPS)

The fundamental principle of X-ray photoelectron spectroscopy (XPS) is Einstein's photoelectric effect, i.e. upon exposing a material to photons of a certain energy, electrons are emitted from the sample. For a photon energy of  $h\nu$ , the kinetic energy of the emitted electrons, measured by an electron energy analyzer, is  $E_{\text{kin}}$ , and the work function is  $\Phi$ . Then the binding energy ( $E_{\text{B}}$ ) of the electrons can be deduced as:  $E_{\text{B}} = h\nu - E_{\text{kin}} - \Phi$ . Thus, emitted electrons with different kinetic energies can be collected and the number of electrons ( $N(E)$ ) with certain  $E_{\text{kin}}$  are recorded by the analyzer when monochromatic photons are used. In Figure 2.1, the relationship of  $N(E)$  vs  $E_{\text{kin}}$  is illustrated, resulting in so-called XP spectra. However, if  $h\nu$  varies,  $E_{\text{kin}}$  will change as well. So for convenience, the spectra of  $N(E)$  vs  $E_{\text{B}}$  are shown usually. Each signal (peak) at characteristic  $E_{\text{B}}$  in the spectra corresponds to a certain occupied electronic state in the atoms, e.g. 1s, 2s, 2p, etc, thus reflecting the electron configuration of the atom. Each element has a characteristic electron configuration, so that the elements existing on the detected material surface can be identified by analyzing the XP spectra. The number of detected electrons ( $N(E)$ ), is proportional to the amount of elements in the irradiated area; thus the chemical composition of the sample can be determined, leading to a quantitative analysis of the surface composition.

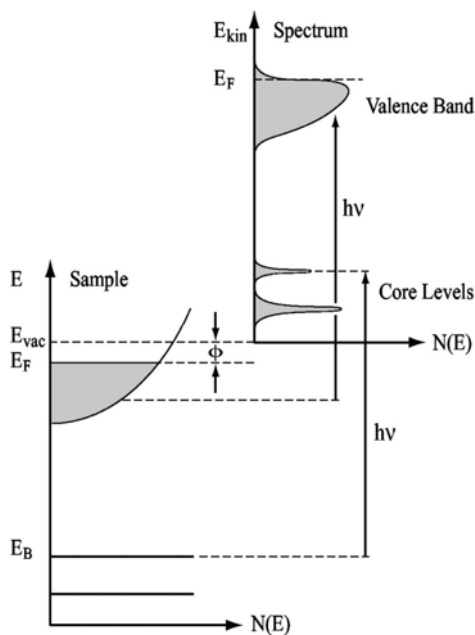


Figure 2.1 Energy scheme of photoelectron spectroscopy

In addition to the chemical composition, XPS is also able to determine the chemical state of an atom. The electron core levels of an atom are influenced by the surrounding chemical environment in the molecule, e.g. coordination and oxidation states. This leads to a binding energy shift of the core level peaks, referred to as chemical shift. The escape depth of the emitted photoelectrons is a few atomic layers, depending on the kinetic energy, thus the information of XPS mostly comes from the surface of the sample, making XPS a suitable technique for surface science research.

## 2.2 Synchrotron radiation

The radiation used in photoelectron spectroscopy basically includes three kinds of sources: (1) vacuum ultraviolet (He I and He II), (2) characteristic X-ray (Mg or Al K $\alpha$ ), and (3) synchrotron radiation. All the PES data in this thesis were obtained by using radiation from the synchrotron source BESSY II in Berlin, Germany (see Figure 2.2). All the core level XPS data were obtained at Beamline U 49/2 PGM1, and the angle-resolved valence-band spectra were measured by Koch et al. from the group Prof. Seyller, at Beamline U 56/2 PGM2.

Synchrotron radiation is generated by radial acceleration of ultra relativistic electrons (1.7 GeV at BESSY II). A broad spectrum of intense light is produced in the synchrotron storage ring with bending magnets, undulators and/or wigglers, ranging from IR to hard X-rays. The generated photons are highly monochromatic, continuously tunable in energy, highly brilliant, and well-defined polarized. In our experiments, we used photon energies, where the photoemission cross section for specific adsorbates core levels is large and the inelastic mean free path is small, leading to high signals of the adsorbates. Due to the remarkably high photon flux used in our experiments, we can measure spectra in a very fast way, e.g. for the C 1s region, typically 10 s. Using synchrotron radiation, also time-dependent investigations are possible, which is not the case for conventional light sources, e.g. Mg or Al K $\alpha$ . In addition, the high energy resolution achieved in the measurements allows distinguishing very small chemical shifts; typically an overall resolution of 200 meV was achieved. This type of high resolution in binding energy and short time-scale allows us to perform so-called 'in-situ' investigation. For example, we investigated the sample during gas exposure, and followed the evolution of the core levels during temperature-programmed heating.



*Figure 2.2: Aerial view of the synchrotron radiation facility BESSY II in Berlin.*

### 2.3 The “synchrotron machine”

All XPS measurements in this thesis were performed using a transportable UHV system, the “synchrotron machine”, which was designed and built in our group.<sup>109</sup> Figure 2.3 shows a picture of the setup without cables. It consists of three main parts: the preparation chamber (on the right side), the analysis chamber (center) and the supersonic molecular beam setup (low left). The preparation chamber is equipped with LEED optics for surface structure analysis, a sputter gun for cleaning the sample, a background gas dosing system, e-beam evaporators and a quartz crystal micro balance (QCM) to calibrate the evaporation of metals. The analysis chamber is equipped with an electron energy analyzer (Omicron EA 125 U7 HR) for XPS measurements, a quadrupole mass spectrometer (Balzers QMA 200) for residual gas analysis and temperature programmed desorption (TPD) measurements. A gas dosing system is attached to the analysis and preparation chambers, allowing background dosing of gases.

The molecular beam consists of three differentially pumped stages. In the first pumping stage, the nozzle with a diameter of 100  $\mu\text{m}$  is located, which can stand temperatures as high as 2000 K. The molecules coming from the nozzle are first collimated by a skimmer, allowing for supersonic conditions.<sup>110</sup> A pneumatic shutter is installed in the second pumping stage for fast on/off switching of the molecular beam. The beam is spatially confined by different apertures between the second and third pumping stage, leading to a molecular beam adapted to the diameter of the sample. Due to the supersonic expansion, the width of the energy distribution of the molecules in a supersonic beam is much smaller than the Maxwell-Boltzmann distribution of an effusive source.<sup>110</sup> The advantage of the supersonic molecular beam is that it allows high local pressures on the sample (up to  $10^{-5}$  mbar), while the background pressure in the chamber is some orders of magnitude lower, as it is spatially confined. In this thesis, the CVD preparation of graphene on Ni(111) is performed by dosing propene through this molecular beam: 45 sccm propene leads to  $\sim 5.7 \times 10^{-6}$  mbar on the Ni(111) surface but only  $2 \times 10^{-8}$  mbar in the analysis chamber.

A horizontal manipulator allows for transporting the sample between the preparation and

the analysis chamber. The sample is mounted at the head of manipulator, and can be cooled to  $\sim 100$  K by liquid nitrogen. A tungsten filament is mounted at the back of the sample, to heat the sample during temperature-programmed XPS (TPXPS) experiments up to 650 K without disturbing the measurements by electric or magnetic stray fields. Direct resistive heating allows temperatures of the sample up to 1500 K.

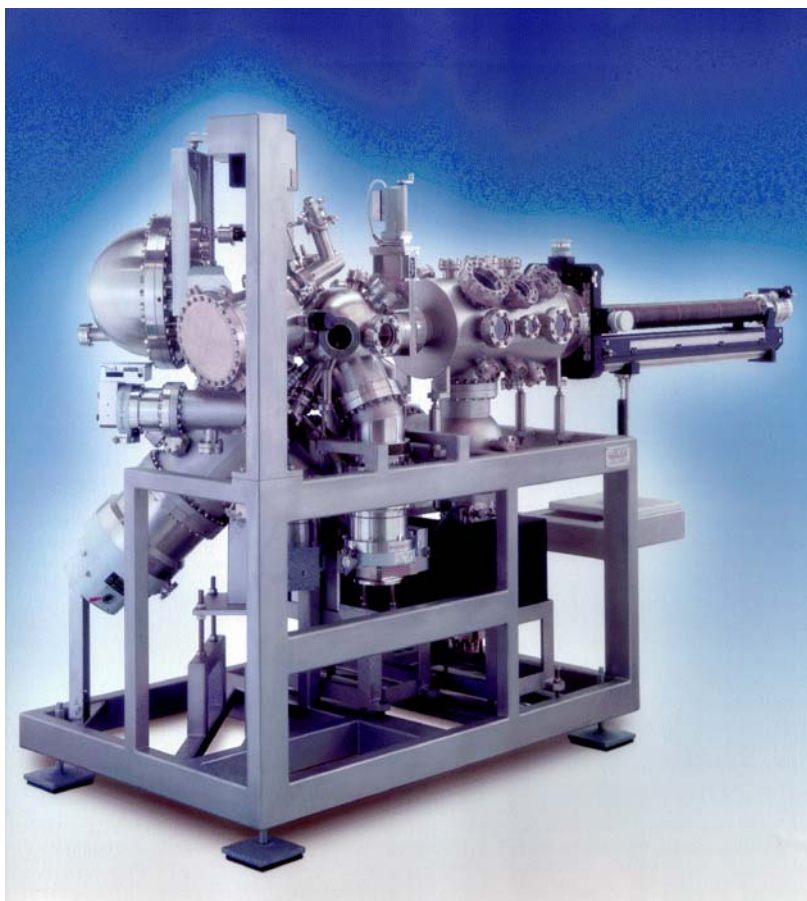


*Figure 2.3: Photograph of the “synchrotron machine”*

## 2.4 TPD and TPXPS

Temperature-programmed desorption (TPD) spectroscopy is a well known technique to observe molecules desorbing from a surface by a quadrupole mass spectrometer during heating of a surface with a constant temperature ramp ( $\beta$ ). The spectra provide insight into the kinetics and thermodynamics of desorption processes and surface reactions. A description of TPD is given by the Polanyi-Wigner equation:<sup>111</sup>

$$\frac{d\Theta}{dT} = \nu \cdot \Theta \cdot \exp\left(-\frac{E_D}{k_B T}\right)$$

with

$\Theta$ : coverage

T: temperature

$\nu$ : preexponential factor

$E_D$ : desorption energy

$k_B$ : Boltzmann constant

n: desorption (reaction) order

The assumption for this equation is that the pumping is high compared to the amount of desorbing molecules, which is valid in most of UHV chambers. Typical desorption is (i) 0<sup>th</sup> order desorption; in this case the desorption rate at a given temperature, which is found independent of the coverage, e.g. the desorption of multilayer adsorbates. (ii) 1<sup>st</sup> order desorption: the desorption rate is proportional to the coverage of adsorbates, e.g. the desorption in the monolayer range with no interactions between adsorbed particles. (iii) 2<sup>nd</sup> order desorption can be found, e.g., in the case of recombinative desorption.

In the case of first order desorption, Redhead proposed a simple way to estimate the desorption energy:<sup>112</sup>

$$E_D = k_B T_m \left( \ln \left( \frac{\nu T_m}{\beta} \right) - 3.51 \right)$$

with

$T_m$ : temperature maximum of the desorption

$\beta$ : heating rate

Temperature-programmed XPS (TPXPS) is derived from TPD, and directly monitors the adsorbates on the surface during heating up by XPS.<sup>113</sup> The main difference between TPXPS and TPD is that not the desorbing particles are analyzed with gas phase, but the reaction and its products on the surface are monitored. The two methods are complementary to each other. One advantage of TPXPS is that TPXPS only monitors the reaction taking place on the surface, because the synchrotron light spot (diameter: 15~100  $\mu\text{m}$ ) is smaller than the sample surface. The signals from the sample holder that can impose a problem in TPD are avoided. In addition, the intermediates existing in a reaction, not associated with desorption, are not accessible by TPD, but (TP)-XPS. On the other hand, hydrogen cannot be quantified by XPS, but can easily be obtained by TPD. For example, in the study of the hydrogenation of graphene, we used TPXPS to investigate the C 1s evolution in the process of hydrogenation and subsequent dehydrogenation, but the problem is the coverage of hydrogen cannot directly be determined by XPS; here the TPD measurements were helpful to identify the amount of hydrogen. And, for the dehydrogenation process, the hydrogen desorption temperatures can not be deduced only from the evolution of C 1s, but with TPD, the direct observation of hydrogen desorption temperatures is achieved.

## 2.5 Low Energy Electron Diffraction (LEED)

LEED is an important science technique for surface structure determination of crystalline materials and for the identification of ordered adsorbate structures on the surface, by diffraction of a collimated beam of low energy electrons.<sup>114</sup> The electrons are emitted from a filament and are accelerated towards the surface with a kinetic energy of 20-500 eV, corresponding to a de-Broglie wave length of 0.3 down to 0.05 nm. Because the wave length of the electrons matches interatomic distances, they are diffracted elastically by the periodically ordered surface or adsorbate atoms, resulting in a reciprocal space image of spots on a fluorescence screen. Due to the low inelastic mean free path electrons, LEED is a surface sensitive tool. This allows us to draw conclusions on the periodicity and lattice constants of surfaces and adsorbate structures.

In this thesis, LEED was used to check the surface structure of Ni(111), when we cleaned the surface, until a clear (111) surface structure was visible without any super structure. Also, after a graphene layer is prepared on the Ni(111) surface, a p(1×1) LEED pattern is observed, indicating no lattice mismatch between graphene and the Ni(111) surface.

## 3. Results

### 3.1 Adsorption structure of graphene on Ni(111) [P1]

The interaction of graphene with adsorbates or with a substrate, in case of supported graphene, can shift and modify its electronic bands and thereby change its physical and chemical properties.<sup>115, 116</sup> For supported graphene, the structure on a particular substrate and the respective interactions are thus of fundamental interest.

In this thesis, Ni(111) was used as substrate to prepare graphene and doped-graphene. Apparently, the adsorption structure and the interaction between graphene and Ni(111), also including the influence on the electronic structure of graphene, are needed to be understood. However, the growth behavior and the structure of graphene on a Ni(111) single crystal surface was heavily debated, with still contradictory results coming both from experiments<sup>55, 61, 75-77</sup> and from density-functional theory (DFT) calculations employing various approaches.<sup>78, 79</sup> In particular, the position of the two carbon atoms in the unit cell, i.e. their “adsorption site” relative to the Ni substrate atoms was a matter of debate. Six different structures, depicted in Figure 3.1, were considered. Early experimental results<sup>55, 61, 75-77</sup> discuss mainly the hcp-fcc and the top-fcc geometries (see Figure 3.1e and 3.1a, respectively); the latter was favored later on by DFT calculations within the Local Density Approximation (LDA).<sup>79</sup> These DFT calculations, however, also point to a second possible low energy conformation, namely the bridge-top geometry (Figure 3.1b).<sup>79</sup> It is noteworthy that in this DFT study van der Waals interactions that are likely to significantly contribute to the binding of graphene to Ni were not taken into account. In fact, LDA calculations resulted in bounded situations due to the wide-known overestimation of the interatomic interactions within the LDA exchange-correlation functional. Note that calculations carried out using the Perdew-Burke-Erzenhof exchange correlation functional resulted in unbound situations, and, in discrepancy with LDA calculations, only one stable conformation, namely hcp-fcc, was found. Interestingly, the published atomic-resolved STM results<sup>55, 75</sup> show discrepancies with respect to the

symmetry of the observed features, which have not been understood in detail yet. Furthermore, an XPS study on the growth of graphene on a Ni film on a W(110) crystal was recently conducted; however, the local geometry was not addressed in detail.<sup>57</sup>

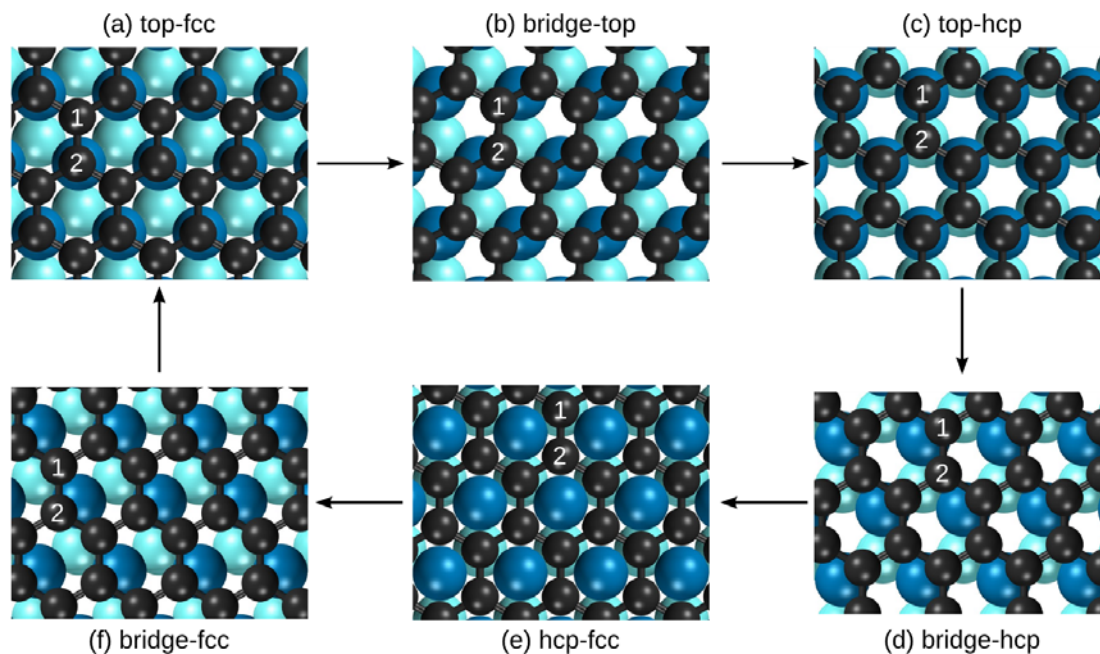


*Figure 3.1 Different adsorption geometries for graphene on Ni(111): a) top-fcc, b) bridge-top, c) top-hcp, d) bridge-hcp, e) hcp-fcc, f) bridge-fcc. The geometries evolve from each other by a shift of the graphene layer against the Ni(111) surface in a direction along a carbon-carbon bond roughly parallel to the diagonal of the displayed surface cut-out.*

We studied the structure of a graphene layer on Ni(111) with a combination of in situ HR-XPS and ab-initio DFT calculations with dispersion correction<sup>117</sup> to take into account van der Waals interactions. Our results indicate that graphene on Ni(111) has two energetically favored geometries, namely the top-fcc and the bridge-top structures displayed in Figure 3.1 a and b; the corresponding layers grow with an almost stochastic distribution, leading to a coexistence of these two adsorption modes on the surface. It is important to note that the DFT calculation was done by S. M. Kozlov from the group of Prof. Dr. Göring at the University of Erlangen-Nürnberg, and the excellent collaboration is gratefully acknowledged.

Experimentally, the growth and structure of graphene on Ni(111) was investigated by in

situ HR-XPS. The clean Ni(111) crystal was exposed to a pressure of  $1 \times 10^{-6}$  mbar of propene at a temperature of 900 K, until saturation of the C 1s intensity. A maximum carbon coverage of 2 ML was observed, corresponding to single layer of graphene. The carbon coverage calibration was done by comparison to a saturated well-ordered ( $\sqrt{7} \times \sqrt{7}$ )R19.1° benzene layer with a carbon coverage of 0.84 ML.<sup>118</sup>

Interestingly, several preparations under identical experimental conditions yielded differing C 1s spectral shapes, but the carbon coverage always indicated a single closed graphene layer. Typical examples of the corresponding XP spectra obtained at 200 K are shown in Figure 3.2: In the topmost spectrum the line shape is dominated by one peak (dashed, green line), whereas the bottom spectrum is dominated by two separated peaks (solid, blue lines) of identical intensity. A large number of preparation procedures always led to spectral shapes, which are composed of a combination of these single peak and double peak spectra, as the middle spectrum. These results can be understood in the light of the DFT calculations for graphene on Ni(111). They yield two energetically equivalent structures: the top-fcc structure and the bridge-top structure. For the bridge-top geometry almost identical shifts of -0.40 eV and -0.36 eV (peak separation: 0.04 eV) are predicted for the two carbon atoms labeled C1 and C2; for the top-fcc geometry shifts of -0.63 eV for the fcc hollow site and -0.19 eV for the on top site (peak separation: 0.44 eV) are obtained, reflecting the strongly differing chemical surrounding; thus for this later geometry two well-separated peaks are expected in the XP spectra.

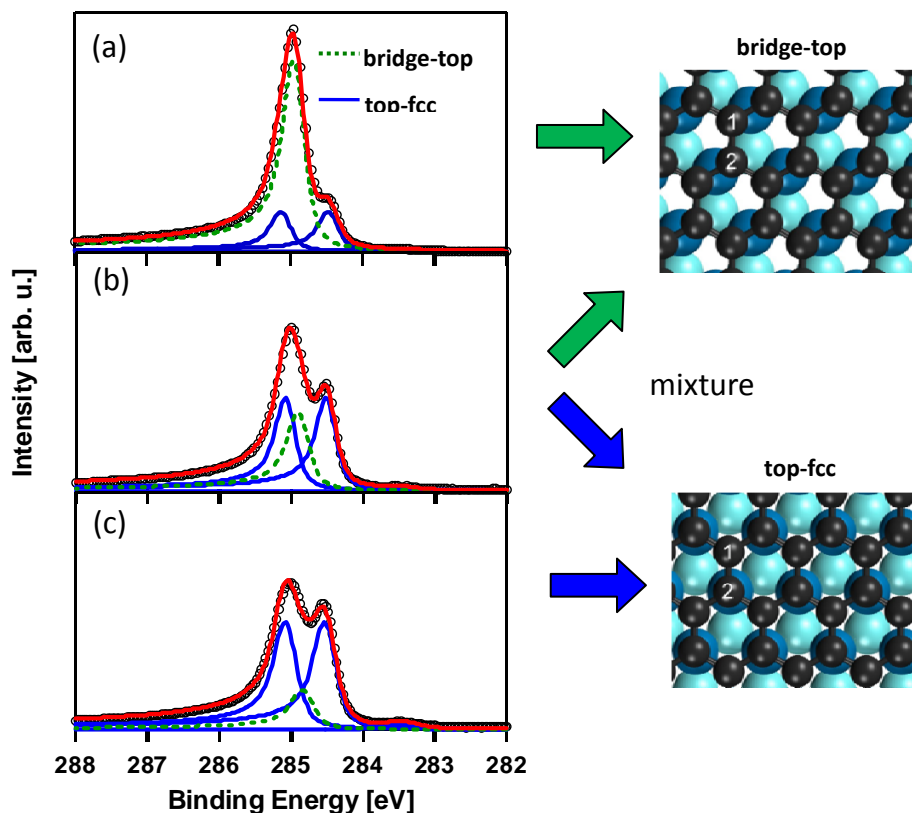


Figure 3.2 C 1s spectra of different graphene layers on Ni(111) ( $h\nu=380$  eV, spectra were taken at  $45^\circ$  off normal emission) and the two most stable structures according to DFT calculation. Shown are preparations with a) mainly graphene in bridge-top geometry; b) a mixture of graphene in bridge-top and top-fcc geometry; c) mainly graphene in top-fcc geometry.

In Figure 3.2 three typical cases are shown: in (a) the bridge-top geometry is the dominating species, in (b) the two geometries coexist, and in (c) the top-fcc geometry dominates the spectrum. The analysis of 20 independent preparations measured at 200 K yielded 40% of bridge-top geometries and 60% top-fcc geometries in average, showing no clear preference for one of the structures. With the energies for the two structures being nearly degenerate, both geometries coexist on the surface, with the relative fractions probably depending on minor defect concentrations (pinning sites) on the surface that at present cannot be identified experimentally. Another possible explanation for the formation of these coexisting structures could be two competing growth modes,<sup>47</sup> leading to the coexistence of these two structures.

### 3.2 N-doped graphene by N ion bombardment [P2]

As discussed in the introduction, hetero-atom doping of graphene is one of the most interesting aspects in graphene research.

One approach to synthesize nitrogen-doped graphene is low energy nitrogen ion bombardment. We start with a highly ordered single-layer graphene on a Ni(111) surface, which was prepared according to literature.<sup>52, 57</sup> Subsequently, this graphene layer was exposed to a beam of low energy nitrogen ions, with energies ranging from 25 to 100 eV. Subsequently, we annealed the nitrogen-bombarded graphene layer to 900 K to allow for a regeneration of the perturbed graphene lattice, leading to nitrogen-doped graphene. Two different doping sites were identified: the substitution of carbon atoms by nitrogen and vacancies in the graphene sheet with pyridinic nitrogen at the edges (see schematic drawing in Figure 3.3), which are denoted as graphitic N and pyridinic N, respectively.

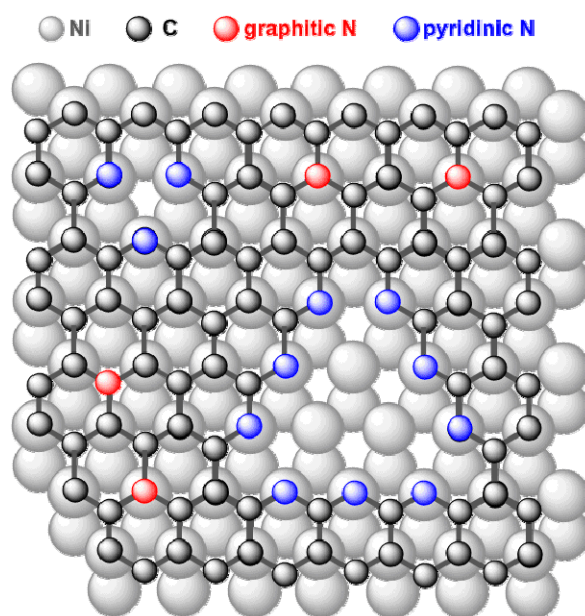


*Figure 3.3 Sketch of nitrogen-doped graphene with the two suggested doping sites, i.e. graphitic and pyridinic nitrogen.*

The preparation steps are monitored in situ with HR-XPS, as shown in Figure 3.4. In the first step a single layer of graphene was prepared on the Ni(111) surface by exposure of the clean surface to propene at 900 K;<sup>52</sup> the corresponding C 1s spectrum is shown as black curve in Figure 3.4a. Thereafter, this layer was exposed to a 50 eV beam of nitrogen

ions at low temperature (<120 K) for 10 minutes. The resulting C 1s and N 1s spectra at 104 K are shown in Figures 3.4a and 3.4b, respectively, as red curves. In comparison to pure graphene, a broader C 1s peak is found, which is attributed to a disturbed graphene lattice induced by nitrogen ion bombardment. The N 1s region exhibits a broad and asymmetric N 1s spectrum, implying the coexistence of several nitrogen species in the sample. To restore an intact graphene structure and desorb excess nitrogen, the nitrogen-bombarded layer was annealed to 900 K. The evolution of the C 1s and N 1s spectra with temperature is shown in Figures 3.4c and 3.4d, respectively. During annealing, the width of the C 1s spectra becomes smaller and the peak shape becomes more symmetric, which suggests that the structure of graphene is indeed recovering. At 900 K, the C 1s spectrum is very similar to that observed for pristine graphene at 900 K.<sup>52</sup> This recovery of the graphene lattice is in line with previous studies of graphene on nickel substrates.<sup>119</sup> In the N 1s spectra a decrease in intensity is found, indicating the desorption of instable nitrogen species (i.e. dinitrogen and nickel nitride) from the near surface region. Finally, at 900 K two well-resolved symmetric peaks are observed at 398.7 and 400.7 eV, which are assigned to pyridinic and graphitic nitrogen, respectively.<sup>99</sup> Cooling down the layer, the C 1s and N 1s spectra are shown in Figures 3.4e and 3.4f. The new species at 285.62 eV in C 1s is assigned to carbon atoms influenced by nitrogen-incorporation, with a coverage of 0.068 ML. The amounts of graphitic and pyridinic nitrogen are determined to be 0.012 and 0.010 ML, respectively.

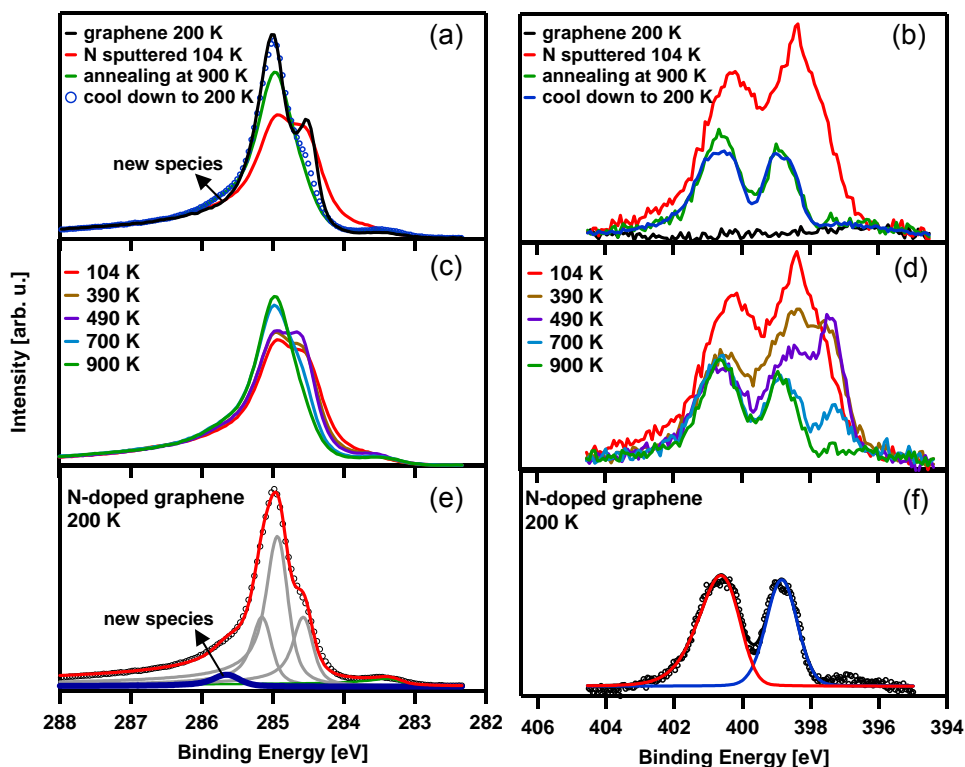


Figure 3.4 (a) C 1s spectra of graphene at 200 K, graphene sputtered with 50 eV nitrogen ions (12  $\mu$ A) for 10 minutes below 120 K (measured at 104 K), nitrogen-sputtered layer after annealing at 900 K, and after cooling down to 200 K. (b) N 1s spectra corresponding to the data in (a). (c,d) Evolution of the C 1s and N 1s spectra of the sputtered sample (50 eV, 12  $\mu$ A, 10 min); photon energy is 380 eV for the C 1s and 500 eV for the N1s spectra. (e,f) Fitting of the C 1s and N1s spectra of nitrogen-doped graphene, measured at 200 K.

Variation of the ion bombardment conditions, such as ion beam energy and bombardment time results in different doping levels and a different branching ratio between pyridinic and graphitic nitrogen, i.e., prolonged bombardment time and higher nitrogen ions would lead to higher nitrogen doping level and more pyridinic type doping sites formed. This is related to the amount of carbon that is lost during the bombardment procedure. Further details are discussed in the article [P2].

### 3.3 N-doped graphene by CVD of pyridine [P3]

This article [P3] was published in cooperation with the groups of Prof. Seyller and Prof. Görling at the University of Erlangen-Nürnberg. The angle-resolved valence-band spectra were measured by R. J. Koch and DFT calculations were performed by F. Viñes. In this CVD method, a single layer of nitrogen-doped graphene was synthesized by exposing a clean Ni(111) surface to pyridine ( $C_5H_5N$ ) at elevated temperatures. As for the preparation of N-doped graphene by nitrogen ion bombardment, here also two N-doping arrangements, the pyridinic-N and graphitic-N were found, but now pyridinic-N is the dominant doping structure. In addition, the N-doping levels are influenced by the growth temperature, i.e. lower temperatures lead to higher nitrogen contents (up to 0.05 ML, i.e. 2.5% at 673 K).

For hetero-atom doped graphene, the impact on the electronic properties of graphene induced by doping is of importance. However, as the effect of the introduction of nitrogen atoms on the electronic properties of graphene might be masked by the well-known strong interaction of graphene with Ni(111), we have also investigated the layers after the intercalation of gold, which is known to decouple graphene from its substrate.<sup>10</sup> The gold intercalation procedures are shown in Figure 3.5, indicating that the effect of N-doping remains present after Au intercalation. The black spectrum shows the the C 1s region of N-doped graphene before gold intercalation, and exhibits a shift to lower binding energy by 0.7 eV after gold intercalation, comparable to other intercalation studies of supported graphene.<sup>10, 120, 121</sup> The N 1s region consists of two species, the pyridinic-N (399.0 eV) and graphitic-N (400.6 eV). The respective structures are shown in the Figure 3.3. After gold intercalation, pyridinic-N shifts to lower binding energy by 0.7 eV, similar to the shift in the C 1s region. Interestingly, graphitic-N keeps the same binding energy after gold intercalation. This discrepancy between pyridinic-N and graphitic-N is due to the different geometries of N atoms in these two doping structures, i.e. pyridinic-N atoms is in the plane of the sheet, leading to a strong interaction with nickel substrate. On the other hand, the graphitic-N atoms are bulked upwards and are out of the plane, thus have less interaction with the substrate. From these considerations, it is concluded that gold intercalation has a

stronger effect on pyridinic-N than on graphitic-N. The significant damping of the Ni 2p signal after gold intercalation, while the intensities of the C 1s and N 1s regions are restored, demonstrates a successful gold intercalation for N-doped graphene.

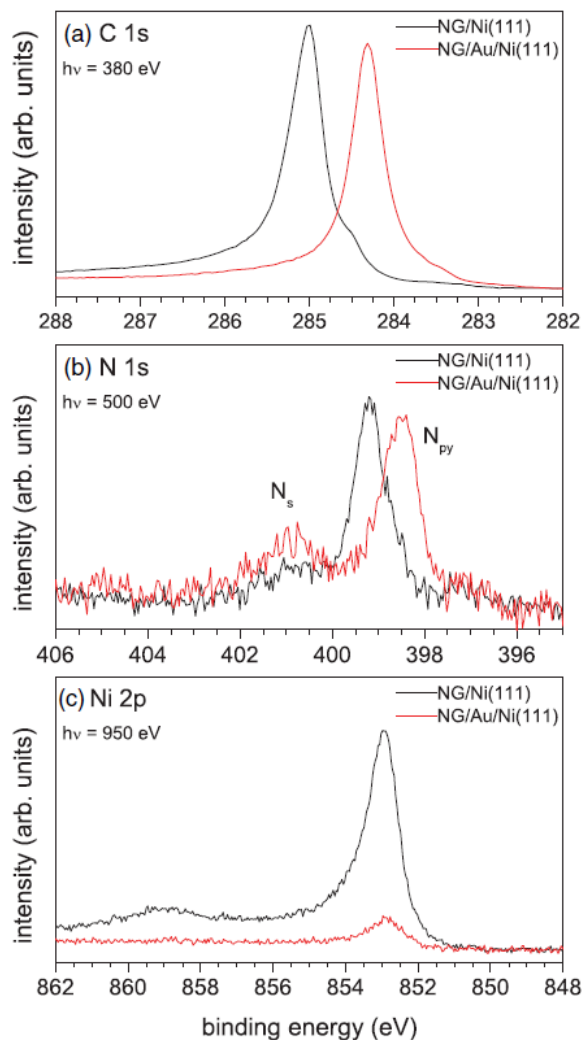


Figure 3.5 HR-XPS of the intercalation of N-doped graphene on Ni(111). Shown are the (a) C 1s, (b) N 1s and (c) the Ni 2p region before and after the intercalation with gold.

The dispersion of the valence bands of N-doped graphene with and without gold intercalation was measured by angle-resolved photoelectron spectroscopy; for a detailed discussion please refer to [P3]. Figure 3.6 shows the energy-dispersion curves (EDCs) at the  $\Gamma$ -point for nitrogen-doped graphene layers with different nitrogen contents. The upper three curves are for N-doped graphene (without gold), and the lower three are the corresponding EDC curves for gold-intercalated N-doped graphene. Before gold

intercalation, the graphene  $\pi$ -band at the  $\Gamma$ -point is shifted significantly to lower energies as the nitrogen content rises. After gold intercalation, the whole  $\pi$ -band shifts to lower binding energies by  $\sim 2$  eV due to decoupling from the nickel substrate. However, the tendency of the  $\pi$ -band shifting to lower binding energies as the nitrogen contents increase is kept as before gold intercalation, implying p-doping for these N-doped graphene layers.

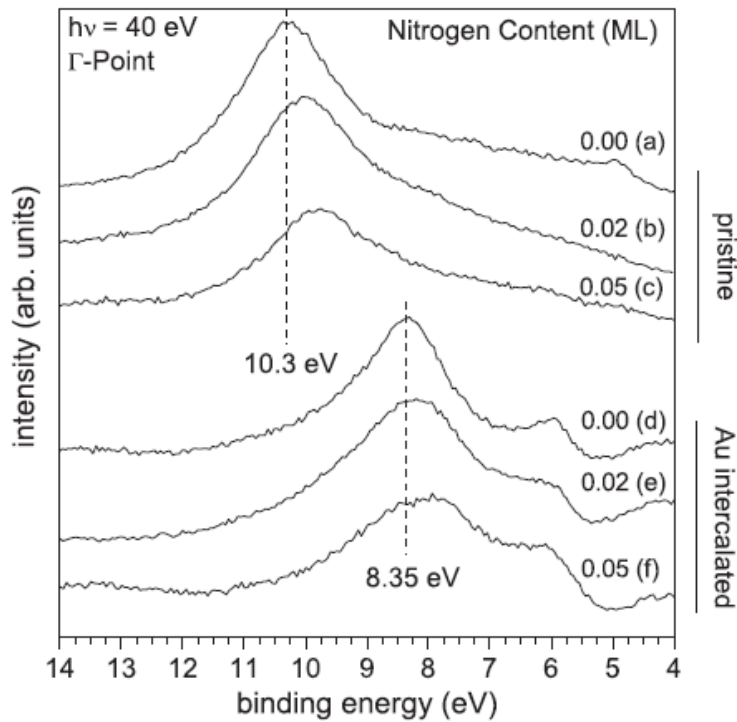


Figure 3.6 Energy distribution curves (EDC) of different ARPES spectra at the  $\Gamma$ -Point. (a) to (c) show spectra from preparations at different temperatures; (d) to (f) show Au intercalated graphene layers.

The changes of the graphene band structure upon doping in the strongly coupled (without Au) and decoupled (with Au) states are interpreted with the help of ab initio density functional (DF) calculations. It shows that the position of  $\pi$ -band at the  $\Gamma$ -point strongly depends on the nitrogen concentration and the doping geometry. For the pyridinic-N configuration, the shift to lower binding energies is due to the surrounding holes/defects. In contrast, the graphitic-N configuration leads to a shift of the  $\pi$ -band to higher binding energies. Further details are discussed in [P3].

### 3.4 B-doped graphene on Ni(111) [P4, P5]

N-doped graphene layers were successfully produced by low energy nitrogen ion bombardment of graphene on Ni(111) and CVD growth on Ni(111) with the precursor molecule pyridine, and two doping configurations, pyridinic-N and graphitic-N were identified, which show shifts in the opposing direction for the  $\pi$ -band of graphene.<sup>88, 97, 98</sup> Boron-doping is also considered as a powerful tool to tune the electronic properties of carbon allotropes, e.g. carbon nanotubes,<sup>122-124</sup> and first results for boron-doped (B-doped) graphene were already presented.<sup>89, 100, 125</sup> However, in these cases, exfoliated graphene or graphite were used, and no CVD growth of B-doped graphene had been reported, implying challenges for the quality of B-doped graphene and for large-scale production. Furthermore results for the incorporation of boron atoms into graphene oxide have also been presented.<sup>126</sup> In this Chapter, production of B-doped graphene on Ni(111) will be addressed and the impact of B-doping on the electronic structure of graphene will be discussed. It is important to note that this work again is collaboration with J. Gebhardt (DFT calculations) and R. J. Koch (valence-band photoelectron spectra).

The B-doped graphene layers were prepared by CVD of the precursor triethylborane (TEB) at elevated temperatures. This approach to the formation of a single layer of B-doped graphene with a high boron content (13 ~ 20%).<sup>107</sup> Alternatively, annealing a boron-containing Ni(111) surface in the presence of propene at 650 ~ 900 K resulted in graphene with a lower boron content (0 ~ 5%).<sup>107</sup>

A scheme of B-doped graphene/Ni(111), with carbon atoms substitutionally replaced by boron atoms, is depicted in Figure 3.7 (a). Figure 3.7 (b) and (c) show typical C 1s and B 1s XP spectra of single layer B-doped graphene prepared by CVD of TEB at 823 K on Ni(111). In the C 1s spectrum, three well-resolved species at 284.31, 283.34, and 282.27 eV are observed; they are attributed to  $sp^2$  hybridized carbon atoms exclusively surrounded by carbon atoms (C1, black), carbon atoms (C2, green) with one neighboring boron atom, and carbon atoms with two neighboring boron atoms (C3, blue), respectively.<sup>107</sup> In the B 1s spectrum, two species are found at 188.00 and 187.31 eV,

which are assigned to elemental boron (B1) atoms on nickel and boron atoms substitutionally incorporated into the carbon network, i.e., bonded to three carbon atoms (B2), respectively.<sup>107</sup> The identification of the C 1s and B 1s species are according to the calculated core level shifts (CLS) of the C 1s and the B 1s states, according to the final-state approximation,<sup>127</sup> in the different possible arrangements (shown in [P4]). In the layer we observe an overall B-doping concentration of ~20%, being much higher than the values obtained for N-doped graphene on Ni(111) prepared by CVD of pyridine.<sup>97</sup>

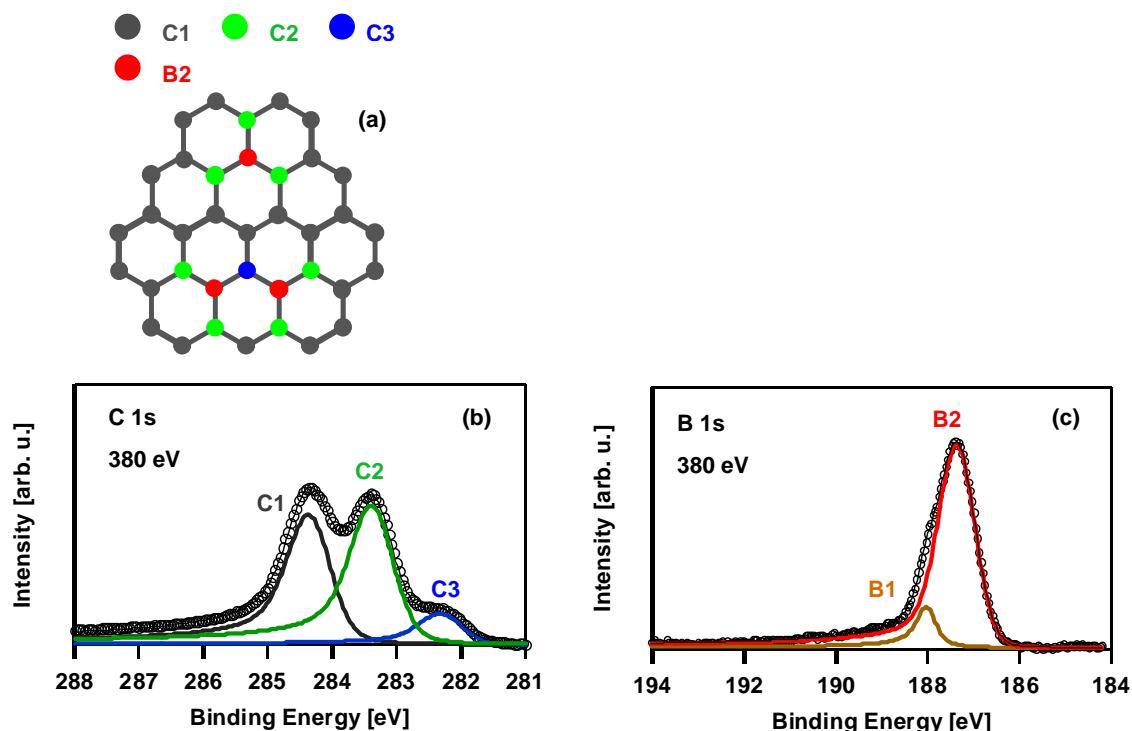


Figure 3.7 (a) Structure of B-doped graphene containing the four relevant atomic species: carbon atoms with exclusively carbon neighbors (C1), carbon atoms bound to two carbon and one boron neighbors (C2), carbon atoms with two boron and one carbon neighbors (C3), and boron atoms substitutionally incorporated into the graphene sheet (B2). (b) and (c) show C 1s and B 1s XP spectra of B-doped graphene on Ni(111) with a boron content of 0.35 ML (20%), respectively. The species B1 in (c) is associated with elemental boron.

We prepared more than ten boron-doped graphene layers on Ni(111) with different B concentration, and here three of them are selected and shown in Figures 3.8(a) and (b) (0.09 ~ 0.35 ML). It is found that C2 and C3 rise while C1 declines as the B concentration

increases from 0.09 to 0.35 ML, confirming that C2 and C3 are the carbon atoms bonded to B atoms. Despite this, we additionally observe a shift of the C1 peak from 285.0 to 284.4 eV with rising boron coverage [see inset of Figure 3.8(a)]. This is due to the fact that boron dopants not only influence the C 1s level of direct neighbors (C2 and C3), but also have an influence on C1, resulting in a shift to lower binding energies and a broadening of the C 1s peak with increasing doping concentration. From a quantitative analysis of the C 1s and B 1s data the combined carbon and boron coverage on the surface was calculated to be around 2 ML, as expected for a closed monolayer of B-doped graphene on Ni(111).

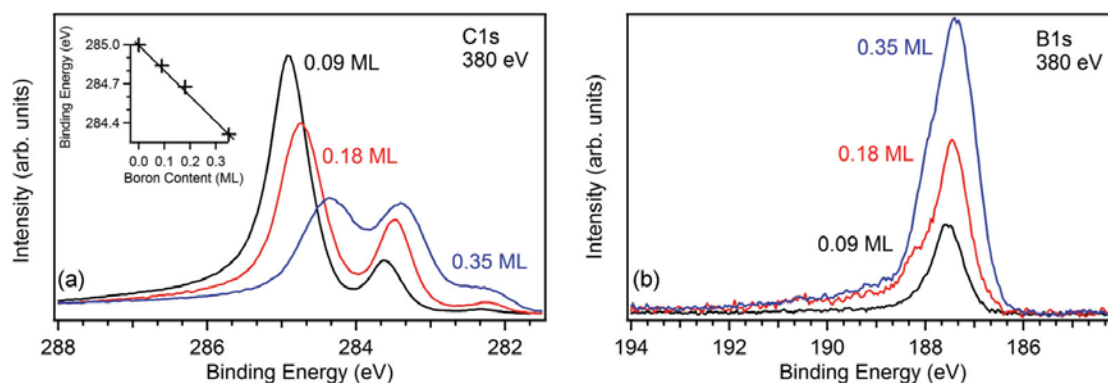


Figure 3.8 High-resolution XPS spectra of (a) the C 1s and (b) the B 1s region of boron-doped graphene with different doping levels. The inset in (a) shows the shift of the graphene C 1s peak with the doping concentration.

To understand the impact of B-doping on the electronic structure of graphene, angle-resolved valence band spectra of B-doped graphene with different B contents were measured. Additionally, also the influence on the adsorption geometry of graphene upon B-doping are discussed in detail in [P4], Figure 3.9 shows the binding energy positions of  $\pi$ -band at the  $\Gamma$ -point for B-doped graphene layers as a function of B content. It is found that the  $\pi$ -band shifts to lower binding energies (towards the Fermi level) as the B concentration rises, implying a p-doping effect for boron incorporation. In contrast to N-doped graphene, only the substitutional doping configuration is found for B-doped graphene, where only leads to p-type graphene materials.

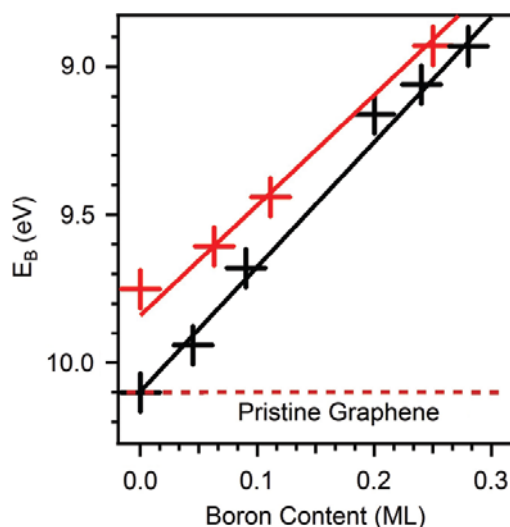


Figure 3.9 Shift of the binding energy  $E_B$  with the boron content of the carbon  $\pi$  band at the  $\Gamma$ -point of graphene on Ni(111) as measured in experiment (black) and predicted by theory (red).

In order to decouple B-doped graphene from nickel substrate, the well-established gold intercalation procedure was tried. As is known, quasi-free-standing graphene is obtained after successful gold intercalation of graphene<sup>10</sup> and N-doped graphene on Ni(111).<sup>88, 97</sup> The decoupling from the metal substrate is especially important for metal-supported doped graphene; otherwise the effect of hetero-atom doping might be obscured by the covalent coupling to the metal. Despite the previous successful intercalation of graphene<sup>10</sup> and N-doped graphene with gold,<sup>88, 97</sup> the gold intercalation of B-doped graphene on Ni(111) shows an unexpected results, i.e. gold does not intercalate B-doped graphene for high boron concentrations (13 ~ 20%); only for lower boron concentrations (~5%) partial intercalation occurs. To obtain detailed insight, we additionally performed DFT calculations, and addressed the differences compared to undoped and N-doped graphene on Ni(111). In the end, we identify the stronger binding of the boron atoms to the nickel substrate as responsible factor of the different gold intercalation behavior in the case of boron doping. The details please refer to [P5].

### 3.5 Hydrogenation of graphene [P6]

In addition to N- and B-doped graphene, hydrogenation of graphene and its corresponding dehydrogenation properties were also of interest. The motivation is based on functionalization of graphene and hydrogen storage,<sup>30, 71, 87, 103, 106, 128 102, 104, 105, 129</sup> as discussed in Chapter 1. Thus, understanding the fundamentals of the adsorption and reaction between hydrogen and graphene is crucial not only due to the interest in hydrogen storage, but also for understanding and tuning its electronic properties.

In this chapter, we investigate the hydrogenation of graphene supported on a Ni(111) surface by in-situ HR-XPS and show that significant differences occur as compared to the hydrogenation of graphene on gold/Ni(111).<sup>130</sup> In our experiments, we find more than two times the amount of carbon is affected by hydrogenation for the Ni(111) supported graphene than for the gold intercalated cases. The thermal evolution of hydrogenated graphene is studied with TPXPS and TPD, showing a two-step dehydrogenation at temperatures of 360 and 600 K. The detailed understanding of this dehydrogenation process is, along with hydrogen storage capacity, a crucial factor for the use of graphene in hydrogen storage applications.

Hydrogenation was performed by exposing a graphene surface to a beam of atomic hydrogen produced by dissociating molecular hydrogen at ~ 2400 K in a tungsten capillary, assembled in a 'hydrogen source' (EFM H from Omicron NanoTechnology).<sup>130, 131</sup> The hydrogen partial pressures during hydrogenation were between  $5 \times 10^{-9}$  and  $1 \times 10^{-6}$  mbar. The hydrogenation time was varied from a few seconds to 6 min.

Figure 3.10 (a) shows the C 1s region of pristine graphene on the Ni(111) surface.<sup>52</sup> To simplify the analysis, we fit the spectra with 3 contributions, carbon atoms that are  $sp^2$  hybridized with a main peak at 284.96 eV and a shoulder at 284.48 eV, and peak due to nickel carbide at 283.56 eV.

Graphene was exposed to atomic hydrogen at 170 K. Figure 3.10 (b) shows the C 1s spectra after exposure to up to 360 L of atomic hydrogen. As the hydrogen exposure increases, the original  $sp^2$  carbon peaks decrease, and simultaneously a new peak at 284.28 eV emerges, reaching saturation at 90 L. Atomic hydrogen is known to react with

graphene to form C-H bonds, transforming  $sp^2$  hybridized carbon to  $sp^3$  hybridized carbon; near edge X-ray absorption fine structure (NEXAFS) experiments showed that C-H bonds are perpendicular to surface,<sup>132</sup> and that every carbon bound to hydrogen is bulked upwards.<sup>105, 132-134</sup> To quantify our observations, we fitted the spectra, as shown in Figure 3.10(c). Obviously, the new species at 284.28 eV is associated with the adsorption of atomic hydrogen. As discussed in [P6], hydrogen intercalation<sup>135, 136</sup> or adsorption between the nickel substrate and graphene are unlikely, and the only possibility is hydrogenation to form C-H bonds, i.e. to  $sp^3$  hybridized carbons with a C 1s peak located at 284.28 eV. Our results are in partial disagreement with earlier work from Ng, et al., who found much lower hydrogen concentrations.<sup>132</sup> The discrepancy is probably due to different sample preparations.

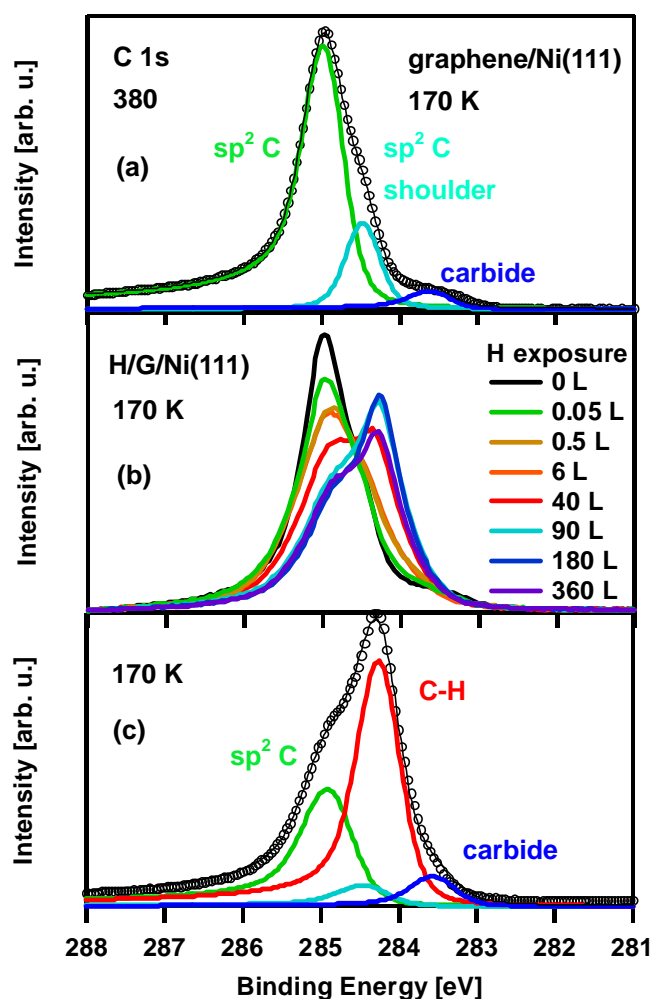
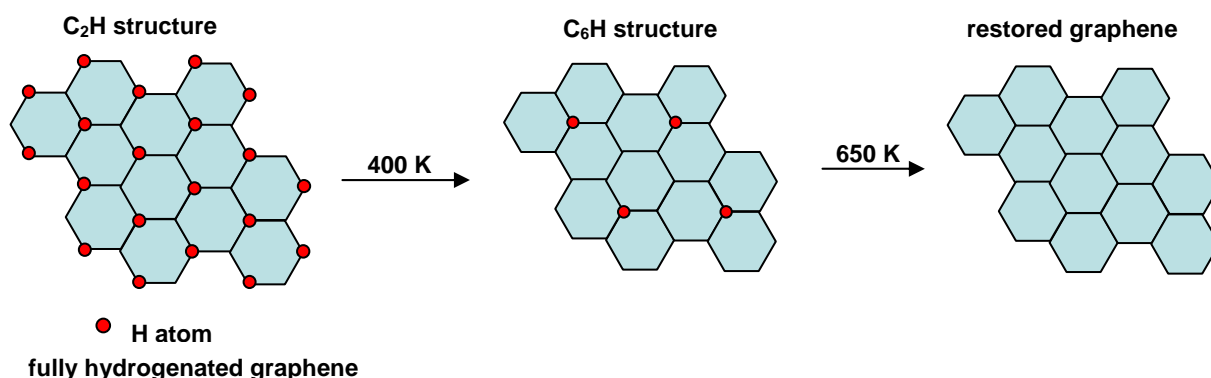


Figure 3.10 (a) Deconvolution of the C 1s spectrum of pristine graphene on Ni(111) at 170 K, green curve ( $sp^2$  C), light blue curve ( $sp^2$  C shoulder), and dark blue curve (carbide). (b)

*Evolution of C 1s region of hydrogenated graphene/Ni(111) as a function of hydrogen exposure (0 - 360 L), measured at 170 K. (c) Deconvolution of the C 1s spectrum of hydrogenated graphene/Ni(111) at 90 L H. Compared to the spectrum of pristine graphene in (a), one new species related with C-H bonds (red curve) is formed.*

For hydrogen storage applications, the properties of the hydrogen release process are also very important, e.g. the hydrogen desorption temperatures. To obtain this information, the dehydrogenation process was investigated with TPD and TP-XPS. TPD is able to determine the desorption temperatures for hydrogen from the graphene surface and also the amount of hydrogen stored on the surface of graphene/Ni(111). In addition, TP-XPS helps to identify the influence of hydrogen on graphene and the intermediate states during dehydrogenation. By combination of these methods, an accurate picture of the hydrogenation of graphene/Ni(111) and dehydrogenation of H/graphene/Ni(111) has been derived, see Figure 3.11. A  $C_6H$  structure forms as the first hydrogenation state at low hydrogen exposures, followed by a  $C_2H$  structure as the second hydrogenation state at high hydrogen exposures. During dehydrogenation, first the  $C_2H$  structures decompose, release hydrogen and transform into  $C_6H$  structures in the temperature region of 300 - 400 K. Subsequently, the  $C_6H$  structure decomposes, starting from 550 K; at 650 K dehydrogenation is completed, resulting in restored graphene layer. The activation energies are derived as 0.81 eV and 1.75 eV for the two dehydrogenation steps.



*Figure 3.11 Schematic model of the dehydrogenation process of hydrogenated graphene/Ni(111).*

In comparison to the hydrogenation of graphene/Au/Ni(111),<sup>130</sup> where a C<sub>4</sub>H polymer-like structure is formed, graphene/Ni(111) has a larger hydrogen storage capacity. The corresponding dehydrogenation on graphene/Au/Ni(111) shows a more complicated behavior. These different results indicate that the hydrogenation of graphene and corresponding dehydrogenation process are strongly influenced by the substrate properties.

## 4. Summary

Graphene is thought to revolutionize the 21st century with many innovative applications, especially in ballistic electronics. In the last years, the controllable tailoring of the properties of graphene have become state-of-the-art in graphene research, and chemical functionalization has been demonstrated as a powerful tool towards this goal. In this thesis, metal-supported graphene and chemically modified graphene, including hetero-atom doping and hydrogenation are discussed, with the experimental results mainly obtained by in-situ HR-XPS.

As a first step, a highly-ordered single graphene layer was successfully synthesized on a Ni(111) surface, and the adsorption structure was studied by HR-XPS and ab initio DFT calculations. We found two coexisting structures of graphene on the Ni(111) surface, namely the bridge-top geometry with the carbon atoms adsorbed equivalently off-center on top of surface Ni atoms, and the top-fcc geometry with one carbon atom adsorbed at an on top position and the other on an hollow-fcc site. The two graphene structures show very similar energies according to DFT calculations. As a consequence, both geometries coexist on the surface, with their relative fractions depending on minor defect concentrations (pinning sites) on the surface.

For the doping of graphene with hetero-atom, the neighbors of carbon in periodic table of elements, nitrogen and boron, were selected. N-doped graphene layers were produced on a Ni(111) surface by low energy nitrogen ion bombardment and CVD growth, both resulting in two different nitrogen doping sites, graphitic and pyridinic nitrogen. For low energy nitrogen ion bombardment, the pristine graphene layer on Ni(111) was exposed to nitrogen ions generated by a sputtering gun, with ion energies from 25 to 100 eV. Annealing the sputtered sample to 900 K to heal the disturbed graphene lattice yielded N-doped graphene. From the XPS data, the relationship between graphene lattice defects and nitrogen doping level as well as the relative population of the two different doping sites was derived. It was shown that it can be tuned in a certain range by variation of the

ion energy and sputtering time.

The CVD synthesis of N-doped graphene on Ni(111), was achieved by pyridine exposure at elevated temperatures. This procedure leads to N-doped graphene layer with less defects (carbon vacancies) compared to low energy nitrogen ion bombardment. We found the pyridinic-N to be the dominant doping arrangement, and that the N doping level can be altered by variation of the growth temperature (up to 2.5%). The electronic properties of N-doped graphene were studied by angle-resolved valence-band spectroscopy and DFT calculations. It was shown that graphitic-N and pyridinic-N have opposite effects on the valence-band (doping types), i.e. n-doping and p-doping, respectively. Furthermore, the DFT calculations by our collaboration partners helped to identify that the p-doping effect from pyridinic-N is caused by the carbon vacancies generated around the pyridinic nitrogen atom. Gold was used to intercalate the N-doped graphene layer, resulting in quasi-free-standing N-doped graphene.

B-doped graphene was synthesized on a Ni(111) surface by CVD and by annealing a B-containing nickel crystal in the presence of propene. In contrast to N-doped graphene, only the substitutional doping geometry is found for B-doped graphene, and the doping levels can be much higher (up to 20%). The electronic structure was studied by angle-resolved photoemission spectroscopy and DFT calculations, showing p-doping for substitutional B-doping. The gold intercalation for B-doped graphene on Ni(111) exhibits a more complicated situation than found for the intercalation of pristine or N-doped graphene on Ni(111). Gold can only partially intercalate the B-doped graphene with low concentrations (0 ~ 5%), and can not intercalate high B-doped graphene layers (13 ~ 20%). From DFT calculations addressing the gold intercalation of pristine graphene, N-doped graphene and B-doped graphene on Ni(111), it is concluded that the strong interactions between boron atoms and nickel substrate are responsible for the difficulties in gold intercalation of B-doped graphene.

Besides doping, hydrogenation of graphene is also studied in this thesis. Atomic hydrogen was used to hydrogenate graphene supported on Ni(111), and the following

dehydrogenation process was investigated by TP-XPS and TPD. The results indicate that  $C_6H$  structure forms as the first hydrogenation state at low hydrogen exposures, and  $C_2H$  structures form as the second stable hydrogenation state at high hydrogen exposures. During the dehydrogenation process,  $C_2H$  structures first decompose, release hydrogen and transform into a  $C_6H$  structure in the temperature region of 300 - 400 K. Subsequently, the  $C_6H$  structures decompose starting from 550 K, and completely dehydrogenate until 650 K, resulting in restored graphene. The activation energies for dehydrogenation are derived as 0.74 eV and 1.75 eV for the two dehydrogenation steps. In comparison to graphene supported on Au/Ni(111), the hydrogen storage capacity is significantly higher for the non-intercalated system.

## 5. Zusammenfassung

Es wird angenommen, dass Graphen und verwandte Materialien das 21. Jahrhundert mit vielen innovativen Anwendungen, vor allem im Bereich der ballistischen Elektronik revolutionieren werden. In den letzten Jahren wurde das kontrollierte Maßschneiden der Eigenschaften von Graphen ein zentrales Forschungsthema und insbesondere die chemische Funktionalisierung wird als besonderes vielversprechender Ansatz betrachtet. In dieser Arbeit wurde Graphen adsorbiert auf Metallen und chemisch funktionalisiertes Graphen, im besonderen Heteroatom-dotiertes und hydrogeniertes Graphen untersucht. Die experimentellen Ergebnisse wurden größtenteils mittels hochaufgelöster in-situ Röntgenphotoelektronenspektroskopie (HR-XPS) gewonnen.

In einem ersten Schritt wurde eine hochgeordnete (1x1) Graphen-Monolage erfolgreich auf einer Ni(111) Oberfläche hergestellt und mittels HR-XPS und ab initio Dichtefunktionaltheorie (DFT)-Rechnungen untersucht. Dabei wurden zwei koexistierende Adsorptionsstrukturen gefunden: in der „bridge-top“ Geometrie sind die beiden Kohlenstoffatome der Graphen-Einheit zelle auf Ni(111) auf äquivalenten brückenartigen Adsorptionsplätzen adsorbiert und in der „top-fcc“ Geometrie ein Kohlenstoffatom direkt auf einem Ni(111) Oberflächenatom und das andere auf einem sogenannten „hollow-fcc“ Adsorptionsplatz. Die DFT Rechnungen zeigen, dass beide Geometrien sehr ähnliche Adsorptionsenergien besitzen und deshalb auf der Oberfläche koexistieren können. Der jeweilige Anteil hängt vermutlich von kleinen Defektkonzentrationen ab.

Zum Dotieren der Graphen-Monolage auf Ni(111) wurden die Nachbarelemente des Kohlenstoffs im Periodensystem, Bor und Stickstoff, gewählt. N-dotiertes Graphen wurde durch Beschuss der Graphen-Monolage mit niederenergetischen Stickstoffionen und durch chemische Gasphasenabscheidung hergestellt. Beide Methoden führten zu unterschiedlich gebundenen Stickstoffen, nämlich graphitischem und pyridinischem Stickstoff. Zur Herstellung mittels Ionenbeschuss wurden mittels einer Ionenkanone

(„Sputtergun“) Stickstoffionen mit kinetischen Energien von 25 bis 100 eV auf das Graphen beschleunigt. Nachfolgendes, kurzzeitiges Erhitzen auf 900 K führte zum Ausheilen von Schäden in der Graphenschicht und somit zu N-dotiertem Graphen. Aus den XPS Daten konnten Zusammenhänge zwischen Graphen-Gitterdefekten und dem Stickstoff-Dotierungsgrad sowie den relativen Besetzungen der beiden unterschiedlich gebundenen Stickstoffe hergestellt werden. Es wurde insbesondere auch gezeigt, dass die relative Konzentration innerhalb gewisser Grenzen durch die Änderung der Ionenenergie und der Beschussdauer eingestellt werden kann.

Die Synthese von N-dotiertem Graphen mittels chemischer Gasphasenabscheidung wurde mit Pyridin als Prekursorgas bei erhöhten Temperaturen erreicht. Dieser Prozess führt, ebenso wie der Beschuss mit niederenergetischen Stickstoffionen, zu N-dotiertem Graphen, allerdings mit weniger Defekten (Kohlenstoff-Leerstellen). Es wurde ermittelt, dass pyridinischer Stickstoff die überwiegende Dotierspezies darstellt und dass sich die erreichte Stickstoffkonzentration durch die Temperatur, bei der die chemische Gasphasenabscheidung durchgeführt wird, in engen Grenzen (bis zu 2,5%), variieren lässt. Die elektronischen Eigenschaften des N-dotierten Graphens wurden im Rahmen einer Kooperation mit Hilfe von winkelaufgelöster Valenzband-Phototoelektronenspektroskopie und DFT Rechnungen bestimmt. Es wurde gezeigt, dass die beiden verschiedenen Dotierspezies, graphitischer und pyridinischer Stickstoff, gegensätzliche Effekte auf die Lage des Valenzband, nämlich n- und p- Dotierung, respektive, hervorrufen. Des Weiteren gelang es mit Hilfe von DFT Rechnungen unserer Kollaborationspartner herauszufinden, dass der p-Dotierungseffekt des pyridinischen Stickstoffs durch die Leerstellen um das Stickstoffatom hervorgerufen wird. In weiteren Untersuchungen wurde Gold zwischen der Ni(111) Oberfläche und dem N-dotierten Graphen interkaliert und auf diese Weise quasi-freistehendes N-dotiertes Graphen erzeugt.

Bor-dotiertes Graphen wurde auf einer Ni(111) Oberfläche durch chemische Gasphasenabscheidung von Triethylboran hergestellt; alternativ konnten geringe Bor-Dotierungen auch durch Heizen eines Bor enthaltendem Nickel Kristall unter

Anwesenheit von Propen erzeugt werden. Im Gegensatz zu N-dotiertem Graphen konnte für die Dotierung mit Bor nur die Geometrie in der Kohlenstoff substituiert wird gefunden werden. Die erreichten Dotier-Konzentrationen (bis zu 20%) waren höher als im Falle der N-Dotierung. Die elektronische Struktur des B-dotierten Graphen wurde wiederum mittels winkelaufgelöster Valenzband-Phototoelektronenspektroskopie und DFT Rechnungen bestimmt; hierbei zeigte sich, dass die Substitution eines Kohlenstoffatoms durch ein Boratom zu einer p-Dotierung führt. Das Interkalieren von Gold zwischen Graphen und Ni(111) führt zu einer komplexeren Situation als dies bei reinem und N-dotiertem Graphen der Fall ist. Bei niedrigdotierten (0 - 5%) Schichten findet eine teilweise Interkalation und bei hochdotierten Schichten (13 - 20%) findet keine Interkalation statt. Aus DFT Rechnungen betreffend die Interkalation von Gold zwischen reinem Graphen, N-dotiertem Graphen und B-dotiertem Graphen, und einer Ni(111) Oberfläche folgt, dass starke Wechselwirkungen zwischen Bor und dem Nickel-Substrat das Interkalieren von B-Dotiertem Graphen erschweren.

Neben dem Dotieren wurde auch das Hydrieren von Graphen in dieser Arbeit untersucht. Graphen auf einem Ni(111) Substrat wurde mit Hilfe von atomarem Wasserstoff hydriert. Anschließend wurde die thermische Dehydrierung mit Temperaturprogrammierten XPS Messungen und mit Temperaturprogrammierter Desorption untersucht. Die Ergebnisse legen nahe, dass sich bei niedrigen Wasserstoffmengen eine stabile  $C_6H$  Struktur ausbildet, während bei hohen Wasserstoffmengen eine stabile  $C_2H$  Struktur entsteht. Bei der Dehydrierung zerfällt zuerst die  $C_2H$  Struktur unter Abspaltung (Desorption) von Wasserstoff in die  $C_6H$  Struktur bei einer Temperatur von 300 – 400 K. Danach zerfällt ab einer Temperatur von 550 K, bis hin zu 650 K, die  $C_6H$  Struktur unter Abspaltung von Wasserstoff zu Graphen. Die Aktivierungsenergien für diese zwei Schritte wurden mit 0,74 und 1,75 eV bestimmt. Im Vergleich zu Gold-interkaliertem Graphen auf Ni(111) ist die Wasserstoff-Speicherkapazität von Graphen auf Ni(111) signifikant höher.

## 6. Acknowledgement

First of all, I would like to thank Professor Hans-Peter Steinrück for providing an excellent environment for scientific work as well as constructive discussions, and thank Dr. Christian Papp for his kind guidance and advice, never failing to improve things.

Secondly, I would like to thank the collaborators, R. J. Koch from the group Prof. Seyller, now at the University of Chemnitz, who measured the valence-band photoelectron spectra, and S. M. Kozlov, F. Viñes, J. Gebhardt from the group Prof. Görling at the University of Erlangen-Nürnberg, who performed the DFT calculations. The excellent cooperation is acknowledged. I also would like to thank all the members of 'sync-group': O. Höfert, K. Gotterbarm, M. P. A. Lorenz, C. Gleichweit and F. Späth. The successful beamtimes can only be performed with your help and excellent team-work.

Thirdly, I would like to thank all the members of in the mechanical workshop for the completion of minor and major repairs. Special thanks to Hans-Peter Bäumlner for the quick help with electronic problems and Bernd Kress for technical support. All employees of the Chair of Physical Chemistry II, I thank for the good working environment and cooperation.

Finally, I would like to thank my family, especially my wife Li Qin and my lovely daughter Juntao Zhao, for their ongoing support during the PhD thesis.

## 7.Literature

- (1) Novoselov, K.S.; Geim, A.K.; Morozov, S.V.; Jiang, D.; Zhang, Y.; Dubonos, S.V.; Grigorieva, I.V.; Firsov, A.A. *Science* **2004**, *306*, 666-669.
- (2) Novoselov, K.S.; Geim, A.K.; Morozov, S.V.; Jiang, D.; Katsnelson, M.I.; Grigorieva, I.V.; Dubonos, S.V.; Firsov, A.A. *Nature* **2005**, *438*, 197-200.
- (3) Zhang, Y.B.; Tan, Y.W.; Stormer, H.L.; Kim, P. *Nature* **2005**, *438*, 201-204.
- (4) Geim, A.K. *Science* **2009**, *324*, 1530-1534.
- (5) Geim, A.K.; Novoselov, K.S. *Nat. Mater.* **2007**, *6*, 183-191.
- (6) Lee, C.; Wei, X.; Kysar, J.W.; Hone, J. *Science* **2008**, *321*, 385-388.
- (7) Novoselov, K.S.; Jiang, Z.; Zhang, Y.; Morozov, S.V.; Stormer, H.L.; Zeitler, U.; Maan, J.C.; Boebinger, G.S.; Kim, P.; Geim, A.K. *Science* **2007**, *315*, 1379.
- (8) Son, Y.W.; Cohen, M.L.; Louie, S.G. *Nature* **2006**, *444*, 347-349.
- (9) Rao, C.N.R.; Matte, H.S.S.R.; Subrahmanyam, K.S.; Maitra, U. *Chem. Sci.* **2012**, *3*, 45-52.
- (10) Varykhalov, A.; Sánchez-Barriga, J.; Shikin, A.M.; Biswas, C.; Vescovo, E.; Rybkin, A.; Marchenko, D.; Rader, O. *Phys. Rev. Lett.* **2008**, *101*, 157601.
- (11) Lehtinen, P.O.; Foster, A.S.; Ayuela, A.; Krasheninnikov, A.; Nordlund, K.; Nieminen, R.M. *Phys. Rev. Lett.* **2003**, *91*, 017202.
- (12) Dedkov, Y.S.; Fonin, M.; Rudiger, U.; Laubschat, C. *Phys. Rev. Lett.* **2008**, *100*, 107602.
- (13) Huang, B.; Li, Z.Y.; Liu, Z.R.; Zhou, G.; Hao, S.G.; Wu, J.; Gu, B.L.; Duan, W.H. *J. Phys. Chem. C* **2008**, *112*, 13442-13446.
- (14) Paul, R.K.; Badhulika, S.; Saucedo, N.M.; Mulchandani, A. *Anal. Chem.* **2012**, *84*, 8171-8178.
- (15) Schedin, F.; Geim, A.K.; Morozov, S.V.; Hill, E.W.; Blake, P.; Katsnelson, M.I.; Novoselov, K.S. *Nat Mater* **2007**, *6*, 652-655.
- (16) Csanyi, G.; Littlewood, P.B.; Nevidomskyy, A.H.; Pickard, C.J.; Simons, B.D. *Nat. Phys.* **2005**, *1*, 42-45.
- (17) Pathak, S.; Shenoy, V.B.; Baskaran, G. *Phys. Rev. B* **2010**, *81*, 085431.
- (18) Wang, X.; Zhi, L.J.; Mullen, K. *Nano Lett.* **2008**, *8*, 323-327.
- (19) Bi, H.; Huang, F.; Liang, J.; Tang, Y.; Lu, X.; Xie, X.; Jiang, M. *J. Mater. Chem.* **2011**, *21*, 17366-17370.
- (20) Li, X.; Fan, L.L.; Li, Z.; Wang, K.L.; Zhong, M.L.; Wei, J.Q.; Wu, D.H.; Zhu, H.W. *Adv. Energy Mater.* **2012**, *2*, 425-429.
- (21) Jeong, H.M.; Lee, J.W.; Shin, W.H.; Choi, Y.J.; Shin, H.J.; Kang, J.K.; Choi, J.W. *Nano Lett.* **2011**, *11*, 2472-2477.
- (22) Zhu, Y.; Murali, S.; Stoller, M.D.; Ganesh, K.J.; Cai, W.; Ferreira, P.J.; Pirkle, A.; Wallace, R.M.; Cychosz, K.A.; Thommes, M., *et al.* *Science* **2011**, *332*, 1537-1541.
- (23) Fan, Z.; Yan, J.; Zhi, L.; Zhang, Q.; Wei, T.; Feng, J.; Zhang, M.; Qian, W.; Wei, F. *Adv. Mater.* **2010**, *22*, 3723-3728.

- (24) Bhardwaj, T.; Antic, A.; Pavan, B.; Barone, V.; Fahlman, B.D. *J. Am. Chem. Soc.* **2010**, *132*, 12556-12558.
- (25) Wang, G.X.; Shen, X.P.; Yao, J.; Park, J. *Carbon* **2009**, *47*, 2049-2053.
- (26) Wu, Z.S.; Ren, W.C.; Xu, L.; Li, F.; Cheng, H.M. *ACS Nano* **2011**, *5*, 5463-5471.
- (27) Avouris, P.; Chen, Z.H.; Perebeinos, V. *Nat. Nanotechnol.* **2007**, *2*, 605-615.
- (28) Wu, Y.; Perebeinos, V.; Lin, Y.-m.; Low, T.; Xia, F.; Avouris, P. *Nano Lett.* **2012**, *12*, 1417-1423.
- (29) Lin, Y.-M.; Dimitrakopoulos, C.; Jenkins, K.A.; Farmer, D.B.; Chiu, H.-Y.; Grill, A.; Avouris, P. *Science* **2010**, *327*, 662.
- (30) Castro Neto, A.H.; Guinea, F.; Peres, N.M.R.; Novoselov, K.S.; Geim, A.K. *Rev. Mod. Phys.* **2009**, *81*, 109-162.
- (31) Emtsev, K.V.; Bostwick, A.; Horn, K.; Jobst, J.; Kellogg, G.L.; Ley, L.; McChesney, J.L.; Ohta, T.; Reshanov, S.A.; Rohrl, J., *et al.* *Nat. Mater.* **2009**, *8*, 203-207.
- (32) Choi, J.; Lee, H.; Kim, S. *J. Phys. Chem. C* **2010**, *114*, 13344-13348.
- (33) Drabinska, A.; Grodecki, K.; Strupinski, W.; Bozek, R.; Korona, K.P.; Wyszomolek, A.; Stepniewski, R.; Baranowski, J.M. *Phys. Rev. B* **2010**, *81*, 245410.
- (34) Qi, Y.; Rhim, S.H.; Sun, G.F.; Weinert, M.; Li, L. *Phys. Rev. Lett.* **2010**, *105*, 085502.
- (35) Riedl, C.; Coletti, C.; Starke, U. *J. Phys. D: Appl. Phys.* **2010**, *43*, 374009.
- (36) Zhou, M.; Wang, Y.L.; Zhai, Y.M.; Zhai, J.F.; Ren, W.; Wang, F.A.; Dong, S.J. *Chem. Eur. J.* **2009**, *15*, 6116-6120.
- (37) Li, X.L.; Wang, H.L.; Robinson, J.T.; Sanchez, H.; Diankov, G.; Dai, H.J. *J. Am. Chem. Soc.* **2009**, *131*, 15939-15944.
- (38) Dikin, D.A.; Stankovich, S.; Zimney, E.J.; Piner, R.D.; Dommett, G.H.B.; Evmemenko, G.; Nguyen, S.T.; Ruoff, R.S. *Nature* **2007**, *448*, 457-460.
- (39) Liu, H.; Zhang, L.; Guo, Y.; Cheng, C.; Yang, L.; Jiang, L.; Yu, G.; Hu, W.; Liu, Y.; Zhu, D. *J. Mater. Chem. C* **2013**, *1*, 3104-3109.
- (40) Pei, S.; Cheng, H.-M. *Carbon* **2011**, *50*, 3210-3228.
- (41) Eda, G.; Fanchini, G.; Chhowalla, M. *Nat. Nanotechnol.* **2008**, *3*, 270-274.
- (42) Wintterlin, J.; Bocquet, M.L. *Surf. Sci.* **2009**, *603*, 1841-1852.
- (43) Matthias, B. *Surf. Sci. Rep.* **2012**, *67*, 83-115.
- (44) Shelton, J.C.; Patil, H.R.; Blakely, J.M. *Surf. Sci.* **1974**, *43*, 493-520.
- (45) Eizenberg, M.; Blakely, J.M. *J. Chem. Phys.* **1979**, *71*, 3467-3477.
- (46) Eizenberg, M.; Blakely, J.M. *Surf. Sci.* **1979**, *82*, 228-236.
- (47) Lahiri, J.; Miller, T.; Adamska, L.; Oleynik, I.I.; Batzill, M. *Nano Lett.* **2011**, *11*, 518-522.
- (48) Klink, C.; Stensgaard, I.; Besenbacher, F.; Lægsgaard, E. *Surf. Sci.* **1995**, *342*, 250-260.
- (49) Coraux, J.; N'Diaye, A.T.; Engler, M.; Busse, C.; Wall, D.; Buckanie, N.; Heringdorf, F.; van Gastel, R.; Poelsema, B.; Michely, T. *New J. Phys.* **2009**, *11*, 023006.
- (50) N'Diaye, A.T.; Coraux, J.; Plasa, T.N.; Busse, C.; Michely, T. *New J. Phys.* **2008**, *10*, 043033.
- (51) N'Diaye, A.T.; Bleikamp, S.; Feibelman, P.J.; Michely, T. *Phys. Rev. Lett.* **2006**, *97*,

- 215501.
- (52) Zhao, W.; Kozlov, S.M.; Höfert, O.; Gotterbarm, K.; Lorenz, M.P.A.; Viñes, F.; Papp, C.; Görling, A.; Steinrück, H.-P. *J. Phys. Chem. Lett.* **2011**, *2*, 759-764.
- (53) Yu, Q.K.; Lian, J.; Siriponglert, S.; Li, H.; Chen, Y.P.; Pei, S.S. *Appl. Phys. Lett.* **2008**, *93*, 113103.
- (54) Li, X.; Zhu, Y.; Cai, W.; Borysiak, M.; Han, B.; Chen, D.; Piner, R.D.; Colombo, L.; Ruoff, R.S. *Nano Lett.* **2009**, *9*, 4359-4363.
- (55) Usachov, D.; Dobrotvorskii, A.M.; Varykhalov, A.; Rader, O.; Gudat, W.; Shikin, A.M.; Adamchuk, V.K. *Phys. Rev. B* **2008**, *78*, 085403.
- (56) Martoccia, D.; Willmott, P.R.; Brugger, T.; Bjorck, M.; Gunther, S.; Schleputz, C.M.; Cervellino, A.; Pauli, S.A.; Patterson, B.D.; Marchini, S., *et al.* *Phys. Rev. Lett.* **2008**, *101*, 126102.
- (57) Grüneis, A.; Kummer, K.; Vyalikh, D.V. *New J. Phys.* **2009**, *11*, 073050.
- (58) Viñes, F.; Neyman, K.M.; Görling, A. *J. Phys. Chem. A* **2009**, *113*, 11963-11973.
- (59) Gao, L.; Guest, J.R.; Guisinger, N.P. *Nano Lett.* **2010**, *10*, 3512-3516.
- (60) Li, X.; Cai, W.; An, J.; Kim, S.; Nah, J.; Yang, D.; Piner, R.; Velamakanni, A.; Jung, I.; Tutuc, E., *et al.* *Science* **2009**, *324*, 1312-1314.
- (61) Gamo, Y.; Nagashima, A.; Wakabayashi, M.; Terai, M.; Oshima, C. *Surf. Sci.* **1997**, *374*, 61-64.
- (62) Sutter, E.; Acharya, D.P.; Sadowski, J.T.; Sutter, P. *Appl. Phys. Lett.* **2009**, *94*, 3.
- (63) Enderlein, C.; Kim, Y.S.; Bostwick, A.; Rotenberg, E.; Horn, K. *New J. Phys.* **2010**, *12*, 033014.
- (64) Cui, Y.; Fu, Q.; Zhang, H.; Tan, D.L.; Bao, X.H. *J. Phys. Chem. C* **2009**, *113*, 20365-20370.
- (65) Algdal, J.; Breitholtz, M.; Kihlgren, T.; Lingren, S.A.; Wallden, L. *Phys. Rev. B* **2006**, *73*, 165409.
- (66) Yang, D.; Velamakanni, A.; Bozoklu, G.; Park, S.; Stoller, M.; Piner, R.D.; Stankovich, S.; Jung, I.; Field, D.A.; Ventrice, C.A., *et al.* *Carbon* **2009**, *47*, 145-152.
- (67) Yang, R.; Huang, Q.S.; Chen, X.L.; Zhang, G.Y.; Gao, H.J. *J. Appl. Phys.* **2010**, *107*, 034305.
- (68) Wang, Y.Y.; Ni, Z.H.; Yu, T.; Shen, Z.X.; Wang, H.M.; Wu, Y.H.; Chen, W.; Wee, A.T.S. *J. Phys. Chem. C* **2008**, *112*, 10637-10640.
- (69) N'Diaye, A.T.; van Gastel, R.; Martínez-Galera, A.J.; Coraux, J.; Hattab, H.; Wall, D.; Meyer zu Heringdorf, F.-J.; Horn-von Hoegen, M.; Gómez-Rodríguez, J.M.; Poelsema, B., *et al.* *New J. Phys.* **2009**, *11*, 113056.
- (70) Eom, D.; Prezzi, D.; Rim, K.T.; Zhou, H.; Lefenfeld, M.; Xiao, S.; Nuckolls, C.; Hybertsen, M.S.; Heinz, T.F.; Flynn, G.W. *Nano Lett.* **2009**, *9*, 2844-2848.
- (71) Elias, D.C.; Nair, R.R.; Mohiuddin, T.M.G.; Morozov, S.V.; Blake, P.; Halsall, M.P.; Ferrari, A.C.; Boukhvalov, D.W.; Katsnelson, M.I.; Geim, A.K., *et al.* *Science* **2009**, *323*, 610-613.
- (72) Li, F.H.; Yang, H.F.; Shan, C.S.; Zhang, Q.X.; Han, D.X.; Ivaska, A.; Niu, L. *J. Mater. Chem.* **2009**, *19*, 4022-4025.
- (73) Malola, S.; Hakkinen, H.; Koskinen, P. *Appl. Phys. Lett.* **2009**, *94*, 043106.

- (74) Wang, X.R.; Li, X.L.; Zhang, L.; Yoon, Y.; Weber, P.K.; Wang, H.L.; Guo, J.; Dai, H.J. *Science* **2009**, *324*, 768-771.
- (75) Bäcker, R.; Hörz, G. *Vacuum* **1995**, *46*, 1101-1104.
- (76) Dedkov, Y.S.; Fonin, M.; Rudiger, U.; Laubschat, C. *Appl. Phys. Lett.* **2008**, *93*, 022509.
- (77) Rosei, R.; De Crescenzi, M.; Sette, F.; Quaresima, C.; Savoia, A.; Perfetti, P. *Phys. Rev. B* **1983**, *28*, 1161-1164.
- (78) Vanin, M.; Mortensen, J.J.; Kelkkanen, A.K.; Garcia-Lastra, J.M.; Thygesen, K.S.; Jacobsen, K.W. *Phys. Rev. B* **2010**, *81*, 081408.
- (79) Fuentes-Cabrera, M.; Baskes, M.I.; Melechko, A.V.; Simpson, M.L. *Phys. Rev. B* **2008**, *77*, 035405.
- (80) Li, X.; Wang, X.; Zhang, L.; Lee, S.; Dai, H. *Science* **2008**, *319*, 1229-1232.
- (81) Wang, X.; Ouyang, Y.; Li, X.; Wang, H.; Guo, J.; Dai, H. *Phys. Rev. Lett.* **2008**, *100*, 206803.
- (82) Gogotsi, Y. *J. Phys. Chem. Lett.* **2011**, *2*, 2509-2510.
- (83) Niyogi, S.; Bekyarova, E.; Hong, J.; Khizroev, S.; Berger, C.; de Heer, W.; Haddon, R.C. *J. Phys. Chem. Lett.* **2011**, *2*, 2487-2498.
- (84) Rao, C.N.R.; Sood, A.K.; Voggu, R.; Subrahmanyam, K.S. *J. Phys. Chem. Lett.* **2010**, *1*, 572-580.
- (85) Sun, Z.; James, D.K.; Tour, J.M. *J. Phys. Chem. Lett.* **2011**, *2*, 2425-2432.
- (86) Kuila, T.; Bose, S.; Mishra, A.K.; Khanra, P.; Kim, N.H.; Lee, J.H. *Prog. Mater Sci.* **2012**, *57*, 1061-1105.
- (87) Liu, H.; Liu, Y.; Zhu, D. *J. Mater. Chem.* **2011**, *21*, 3335-3345.
- (88) Usachov, D.; Vilkov, O.; Grüneis, A.; Haberer, D.; Fedorov, A.; Adamchuk, V.K.; Preobrajenski, A.B.; Dudin, P.; Barinov, A.; Oehzelt, M., *et al.* *Nano Lett.* **2011**, *11*, 5401-5407.
- (89) Panchakarla, L.S.; Subrahmanyam, K.S.; Saha, S.K.; Govindaraj, A.; Krishnamurthy, H.R.; Waghmare, U.V.; Rao, C.N.R. *Adv. Mater.* **2009**, *21*, 4726-4730.
- (90) Jin, Z.; Yao, J.; Kittrell, C.; Tour, J.M. *ACS Nano* **2011**, *5*, 4112-4117.
- (91) Palnitkar, U.A.; Kashid, R.V.; More, M.A.; Joag, D.S.; Panchakarla, L.S.; Rao, C.N.R. *Appl. Phys. Lett.* **2010**, *97*, 063102.
- (92) Cheianov, V.V.; Fal'ko, V.; Altshuler, B.L. *Science* **2007**, *315*, 1252-1255.
- (93) Gorjizadeh, N.; Kawazoe, Y. *J. Nanomater.* **2010**, *2010*, 513501.
- (94) Biel, B.; Triozon, F.o.; Blase, X.; Roche, S. *Nano Lett.* **2009**, *9*, 2725-2729.
- (95) Wei, D.C.; Liu, Y.Q.; Wang, Y.; Zhang, H.L.; Huang, L.P.; Yu, G. *Nano Lett.* **2009**, *9*, 1752-1758.
- (96) Zhao, L.; He, R.; Rim, K.T.; Schiros, T.; Kim, K.S.; Zhou, H.; Gutiérrez, C.; Chockalingam, S.P.; Arguello, C.J.; Pálová, L., *et al.* *Science* **2011**, *333*, 999-1003.
- (97) Koch, R.J.; Weser, M.; Zhao, W.; Viñes, F.; Gotterbarm, K.; Kozlov, S.M.; Höfert, O.; Ostler, M.; Papp, C.; Gebhardt, J., *et al.* *Phys. Rev. B* **2012**, *86*, 075401.
- (98) Zhao, W.; Höfert, O.; Gotterbarm, K.; Zhu, J.F.; Papp, C.; Steinrück, H.P. *J. Phys. Chem. C* **2012**, *116*, 5062-5066.

- (99) Kim, K.J.; Lee, H.; Choi, J.; Jung, M.C.; Shin, H.J.; Kang, T.H.; Kim, B.; Kim, S. *J. Phys.-Condes. Matter.* **2010**, *22*, 045005.
- (100) Tang, Y.-B.; Yin, L.-C.; Yang, Y.; Bo, X.-H.; Cao, Y.-L.; Wang, H.-E.; Zhang, W.-J.; Bello, I.; Lee, S.-T.; Cheng, H.-M., *et al.* *ACS Nano* **2012**, *6*, 1970-1978.
- (101) Lin, T.; Huang, F.; Liang, J.; Wang, Y. *Energy Environ. Sci.* **2010**, *4*, 862-865.
- (102) Bostwick, A.; McChesney, J.L.; Emtsev, K.V.; Seyller, T.; Horn, K.; Kevan, S.D.; Rotenberg, E. *Phys. Rev. Lett.* **2009**, *103*, 056404.
- (103) Sofo, J.O.; Chaudhari, A.S.; Barber, G.D. *Phys. Rev. B* **2007**, *75*, 153401.
- (104) Flores, M.Z.S.; Autreto, P.A.S.; Legoas, S.B.; Galvao, D.S. *Nanotechnology* **2009**, *20*, 465704.
- (105) Balog, R.; Jorgensen, B.; Nilsson, L.; Andersen, M.; Rienks, E.; Bianchi, M.; Fanetti, M.; Laegsgaard, E.; Baraldi, A.; Lizzit, S., *et al.* *Nature Mater. Lett.* **2010**, *9*, 315-319.
- (106) Tozzini, V.; Pellegrini, V. *Phys. Chem. Chem. Phys.* **2013**, *15*, 80-89.
- (107) Gebhardt, J.; Koch, R.J.; Zhao, W.; Höfert, O.; Gotterbarm, K.; S.Mammadov; Papp, C.; Görling, A.; Steinrück, H.-P.; Seyller, T. *Phys. Rev. B* **2013**, *87*, 155437.
- (108) Wang, H.; Maiyalagan, T.; Wang, X. *ACS Catal.* **2012**, *2*, 781-794.
- (109) Denecke, R.; Kinne, M.; Whelan, C.M.; Steinrück, H.-P. *Surf. Rev. Lett.* **2002**, *9*, 797-801.
- (110) Scoles, G. *Oxford University Press, New York* **1988**, Vol. 1.
- (111) de Jong, A.M.; Niemantsverdriet, J.W. *Surf. Sci.* **1990**, *233*, 355-365.
- (112) Redhead, P.A. *Vacuum* **1962**, *12*, 203-211.
- (113) Baraldi, A.; Barnaba, M.; Brena, B.; Cocco, D.; Comelli, G.; Lizzit, S.; Paolucci, G.; Rosei, R. *J. Electron Spec. Rel. Phen.* **1995**, *76*, 145-149.
- (114) Davisson, C.; Germer, L.H. *Phys. Rev.* **1927**, *30*, 705-740.
- (115) Oida, S.; McFeely, F.R.; Hannon, J.B.; Tromp, R.M.; Copel, M.; Chen, Z.; Sun, Y.; Farmer, D.B.; Yurkas, J. *Phys. Rev. B* **2010**, *82*, 041411.
- (116) Zhou, S.Y.; Gweon, G.H.; Fedorov, A.V.; First, P.N.; De Heer, W.A.; Lee, D.H.; Guinea, F.; Neto, A.H.C.; Lanzara, A. *Nat. Mater.* **2007**, *6*, 770-775.
- (117) Ortman, F.; Bechstedt, F.; Schmidt, W.G. *Phys. Rev. B* **2006**, *73*, 205101.
- (118) Papp, C.; Fuhrmann, T.; Trankenschuh, B.; Denecke, R.; Steinrück, H.-P. *Phys. Rev. B* **2006**, *73*, 235426.
- (119) Karoui, S.; Amara, H.; Bichara, C.; Ducastelle, F. *ACS Nano* **2010**, *4*, 6114-6120.
- (120) Speck, F.; Jobst, J.; Fromm, F.; Ostler, M.; Waldmann, D.; Hundhausen, M.; Weber, H.B.; Seyller, T. *Appl. Phys. Lett.* **2011**, *99*, 122106-122103.
- (121) Emtsev, K.V.; Speck, F.; Seyller, T.; Ley, L.; Riley, J.D. *Phys. Rev. B* **2008**, *77*, 155303.
- (122) Yang, L.; Jiang, S.; Zhao, Y.; Zhu, L.; Chen, S.; Wang, X.; Wu, Q.; Ma, J.; Ma, Y.; Hu, Z. *Angew. Chem.-Int. Edit.* **2011**, *50*, 7132-7135.
- (123) Panchakarla, L.S.; Govindaraj, A.; Rao, C.N.R. *ACS Nano* **2007**, *1*, 494-500.
- (124) Zheng, B.; Hermet, P.; Henrard, L. *ACS Nano* **2010**, *4*, 4165-4173.
- (125) Kim, Y.A.; Fujisawa, K.; Muramatsu, H.; Hayashi, T.; Endo, M.; Fujimori, T.; Kaneko, K.; Terrones, M.; Behrends, J.; Eckmann, A., *et al.* *ACS Nano* **2012**, *6*, 6293-6300.

- (126) Sheng, Z.-H.; Gao, H.-L.; Bao, W.-J.; Wang, F.-B.; Xia, X.-H. *J. Mater. Chem.* **2012**, *22*, 390-395.
- (127) Köhler, L.; Kresse, G. *Phys. Rev. B* **2004**, *70*, 165405.
- (128) Fowler, J.D.; Allen, M.J.; Tung, V.C.; Yang, Y.; Kaner, R.B.; Weiller, B.H. *ACS Nano* **2009**, *3*, 301-306.
- (129) Dan, Y.; Lu, Y.; Kybert, N.J.; Luo, Z.; Johnson, A.T.C. *Nano Lett.* **2009**, *9*, 1472-1475.
- (130) Haberer, D.; Giusca, C.E.; Wang, Y.; Sachdev, H.; Fedorov, A.V.; Farjam, M.; Jafari, S.A.; Vyalikh, D.V.; Usachov, D.; Liu, X., *et al. Adv. Mater.* **2011**, *23*, 4497-4503.
- (131) Balog, R.; Jørgensen, B.; Wells, J.; Lægsgaard, E.; Hofmann, P.; Besenbacher, F.; Hornekær, L. *J. Am. Chem. Soc.* **2009**, *131*, 8744-8745.
- (132) Ng, M.L.; Balog, R.; Hornekær, L.; Preobrajenski, A.B.; Vinogradov, N.A.; Mårtensson, N.; Schulte, K. *J. Phys. Chem. C* **2010**, *114*, 18559-18565.
- (133) Hornekær, L.; Rauls, E.; Xu, W.; Šljivančanin, Ž.; Otero, R.; Stensgaard, I.; Lægsgaard, E.; Hammer, B.; Besenbacher, F. *Phys. Rev. Lett.* **2006**, *97*, 186102.
- (134) Hornekær, L.; Šljivančanin, Ž.; Xu, W.; Otero, R.; Rauls, E.; Stensgaard, I.; Lægsgaard, E.; Hammer, B.; Besenbacher, F. *Phys. Rev. Lett.* **2006**, *96*, 156104.
- (135) Riedl, C.; Coletti, C.; Iwasaki, T.; Zakharov, A.A.; Starke, U. *Phys. Rev. Lett.* **2009**, *103*, 246804.
- (136) Watcharinyanon, S.; Virojanadara, C.; Osiecki, J.R.; Zakharov, A.A.; Yakimova, R.; Uhrberg, R.I.G.; Johansson, L.I. *Surf. Sci.* **2011**, *605*, 1662-1668.

## 8. Appendix: P1 – P6

[P1] Graphene on Ni(111): Coexistence of Different Surface Structures

**W. Zhao**, S. M. Kozlov, O. Höfert, K. Gotterbarm, M. P. A. Lorenz, F. Viñes, C. Papp, A. Görling, and H.-P. Steinrück

[J. Phys. Chem. Lett., 2 \(2011\) 759](#)

[P2] Production of Nitrogen-Doped Graphene by Low-Energy Nitrogen Implantation

**W. Zhao**, O. Höfert, K. Gotterbarm, J. F. Zhu, C. Papp, and H.-P. Steinrück

[J. Phys. Chem. C, 116 \(2012\) 5062](#)

[P3] Growth and electronic structure of nitrogen-doped graphene on Ni(111)

R. J. Koch, M. Weser, **W. Zhao**, F. Viñes, K. Gotterbarm, S. M. Kozlov, O. Höfert, M. Ostler, C. Papp, J. Gebhardt, H. P. Steinrück, A. Görling, and T. Seyller

[Phys. Rev. B, 86 \(2012\) 075401](#)

[P4] Growth and electronic structure of boron doped graphene

J. Gebhardt, R. J. Koch, **W. Zhao**, O. Höfert, K. Gotterbarm, S. Mammadov, C. Papp, A. Görling, H.-P. Steinrück, and T. Seyller

[Phys. Rev. B, 87 \(2013\) 155437](#)

[P5] Gold intercalation of boron-doped graphene on Ni(111): XPS and DFT Study

**W. Zhao**, J. Gebhardt, K. Gotterbarm, O. Höfert, C. Gleichweit, C. Papp, A. Görling, and H.-P. Steinrück

[J. Phys.: Condens. Matter., 25 \(2013\) 445002](#)

[P6] Investigation of the hydrogenation and dehydrogenation of graphene/Ni(111)

**W. Zhao**, F. Späth, K. Gotterbarm, C. Gleichweit, H.-P. Steinrück, and C. Papp

In preparation.

P6



# Investigation of the hydrogenation and dehydrogenation of graphene / Ni(111)

W. Zhao, F. Späth, K. Gotterbarm, C. Gleichweit, H.-P. Steinrück and C. Papp

*Lehrstuhl für Physikalische Chemie II, Universität Erlangen-Nürnberg, Egerlandstr. 3, 91058  
Erlangen*

## **Abstract**

Understanding the adsorption and reaction between hydrogen and graphene is of fundamental importance for developing graphene-based hydrogen storage and chemical functionalization of graphene by hydrogenation. Herein, single layer graphene prepared on Ni(111) is exposed to atomic hydrogen, yielding hydrogenated graphene. Applying high-resolution X-ray photoemission spectroscopy, the impact of the hydrogenation on graphene was investigated in detail. Subsequently, the dehydrogenation process was investigated by temperature-programmed XPS and temperature programmed desorption to elucidate the dehydrogenation process and to determine the hydrogen coverages and dehydrogenation energies of the two different desorption states. Additionally, we propose a model for the adsorption geometry of hydrogen on graphene.

## Introduction

Hydrogen storage based on graphene materials has attracted considerable attention in recent years, due to its promising performances in hydrogen storage capacity and control of storing/releasing hydrogen at proper temperatures (300 ~ 600 K).<sup>1</sup> The product obtained after fully hydrogenating graphene ( $C_xH_x$ ), known as graphane,<sup>2</sup> shows a remarkable high hydrogen storage capacity of 8.3 w.t.%, which is close to the objectives of the US Department of Energy for hydrogen storage (9 wt% by 2015).<sup>3</sup> Furthermore, since graphene was found,<sup>4</sup> its chemical functionalization has been considered as an important method to tailor the electronic and chemical properties for functional device and gas sensors applications.<sup>5-7</sup> <sup>8</sup> It was demonstrated that reversible hydrogenation allows for controlling the electrical transport properties of single layer graphene.<sup>3,9</sup> Electronically, graphene is a zero-gap semi-metal, and graphane is an insulator with a band-gap of 3.5 eV.<sup>2</sup> The electronic properties of hydrogenated graphene are strongly affected by the hydrogen coverage and chemisorption pattern.<sup>10, 11</sup> To this end, understanding the fundamentals of the adsorption and reaction between hydrogen and graphene is crucial, for hydrogen storage and also for understanding and tuning its electronic properties.

A recent study of the hydrogenation of graphene supported on gold/Ni(111) proposed a  $C_4H$ -type structure, with a hydrogen saturation coverage of 25%.<sup>12</sup> Investigations of hydrogen chemisorbed on graphene supported on SiC show a similar behavior as observed for the chemisorption of atomic hydrogen on graphite, i.e. the formation of C-H monomers, dimers and clusters, with saturation coverages of up to 40%.<sup>13-15</sup> Ng et.al found that graphene supported by different transition metals adsorbs hydrogen in various ways, depending on the substrate: On graphene on Ir(111) and Pt(111), hydrogen atoms adsorb preferably on carbon atoms in the valleys, forming graphane-like structure. In the case of the commensurate structure of graphene on Ni(111) an adsorption on every third carbon atom situated on the on top substrate sites is found<sup>16</sup> The hydrogen storage capacity on these systems can be remarkably high, e.g. as much as 60 % for H/Graphene/Pt(111); on the other hand, on Ni(111) and gold intercalated graphene on Ni(111) only coverages of 17%<sup>16</sup> and 25%<sup>12</sup> were reached, respectively. Obviously, the substrate plays an important role in the hydrogenation of supported graphene. In particular for hydrogen storage applications, the thermal evolution and the kinetics of hydrogen desorption/releasing is highly important. Despite this relevance, no studies about the dehydrogenation process of hydrogenated graphene supported on metals, e.g. in our case of Ni(111), have not been conducted yet. Herein, we revisit the hydrogenation of

graphene supported on a Ni(111) surface by in-situ high resolution X-ray photoemission spectroscopy (XPS) and show that significant differences occur in comparison to the hydrogenation of graphene on gold/Ni(111).<sup>12</sup> In our experiments we observed that more than twice the amount of carbon is affected by hydrogenation; in addition, also other significant differences are found compared to earlier measurements.<sup>16</sup> Special attention is paid to the dehydrogenation of hydrogenated graphene, i.e. the release of hydrogen from the storage material, as this is a crucial factor for the use of graphene in hydrogen storage applications. The dehydrogenation was studied with temperature-programmed XPS (TP-XPS) and temperature-programmed desorption (TPD); from both methods two desorption states at 360 and 600 K were identified. Furthermore, we propose an adsorption geometry of hydrogen on graphene and give estimated for the activation energies for the desorption.

## Experimental

The XPS experiments were performed in a transportable UHV apparatus connected to beamline U49/2 PGM1 at BESSY II of the Helmholtz-Zentrum Berlin. Graphene was prepared by exposing a Ni(111) crystal to  $1 \times 10^{-6}$  mbar of propene at 650 K until saturation, with subsequent annealing to 900 K, to form single layer of graphene on the Ni(111) surface.<sup>17</sup> Hydrogenation was performed by exposing the graphene surface to a beam of atomic hydrogen produced by dissociating molecular hydrogen at  $\sim 2400$  K in a tungsten capillary, (EFM H from Omicron Nano Technology). The hydrogen partial pressures during hydrogenation were in the range from  $5 \times 10^{-9}$  to  $1 \times 10^{-6}$  mbar. The hydrogenation time was varied from a few seconds to 6 min. It is important to note that the cracking efficiency of hydrogen is nearly 100% at the temperature we used. The given hydrogen pressures are background pressures and thus are lower than in the hydrogen beam. During hydrogenation, the sample was kept at 170 K. For the TPXPS experiments a linear heating rate of 0.5 K/s was used. The C 1s spectra were recorded using a photon energy of 380 eV, with a resolution of  $\sim 200$  meV. The carbon coverage is calibrated by comparison to a saturated well-ordered  $(\sqrt{7} \times \sqrt{7})R19.1^\circ$  benzene layer with a known carbon coverage of 0.86 ML,<sup>18</sup> (where 1 ML corresponds to one carbon atom per substrate nickel atom); note that a perfect graphene layer corresponds to a coverage of 2 ML, as it contains two carbon atoms per (1x1) substrate unit cell. During the TPD experiments, the background pressure in the chamber was below  $4 \times 10^{-10}$  mbar. A linear heating ramp of 3 K/s was used and mass  $m/e = 2$  was measured in the quadruple mass spectrometer (QMS) to detect molecular hydrogen.

## Results and Discussions

Fig. 1 (a) shows the C 1s region of a pristine saturated graphene layer on the Ni(111) surface.<sup>17</sup> In Fig. 1 (b) a series of C 1s spectra is shown, measured after exposure of the graphene layer to different amounts of atomic hydrogen. As the hydrogen exposure increases, the original graphene signal decreases and simultaneously a new peak at 284.28 eV emerges, reaching saturation at 90 L. This change is attributed to the reactions of the atomic hydrogen with graphene to form C-H bonds, transforming  $sp^2$  hybridized carbon to  $sp^3$  hybridized carbon. This interpretation is in line with NEXAFS experiments that show that C-H bonds are formed, which are perpendicular to surface,<sup>16</sup> and that every carbon atom bound to a hydrogen is bulked upward.<sup>11, 16</sup>

To quantify these observations we fitted the spectra: At first we shortly want to discuss the fit of pristine graphene, which is known to show two different adsorption geometries, namely bridge-top and top-fcc that coexist on the surface.<sup>17</sup> To simplify the quantitative analysis in Fig. 1 we fitted the spectra of pristine graphene (plus nickel carbide) with three contributions: the  $sp^2$  hybridized carbons atoms due to graphene are represented by a main peak at 284.96 eV and a shoulder at 284.48 eV, and the carbon atoms from nickel carbide are fitted with a peak at 283.56 eV. This fit does not take into account the two different adsorption geometries. Alternatively, we also performed the fitting method with (three) separate peaks for the bridge-top and top-fcc geometry as described in Ref. 17, and found that it lead to the same results, although with a higher error bar. For fitting the spectra after hydrogenation always the envelopes of the two-peak fit or the three-peaks fits were used (i.e. the peak plus shoulder, or the three peaks with fixed intensity ratios) to account the fraction of non-hydrogenated carbons atoms.

The new peak at 284.28 eV observed after exposure to atomic hydrogen principally can be associated with different scenarios: (i) Hydrogen atoms intercalate under the graphene layer, resulting in decoupled carbon species from nickel substrate, as observed for graphene on SiC.<sup>19, 20</sup> (ii) Hydrogen atoms adsorb on graphene from both sides, forming a graphane-like structure. (iii) Hydrogen atoms adsorbing on graphene only from the top side. In the following, we will shortly argue why the answers (i) and (ii) are unlikely: The intercalation of hydrogen has not been observed for graphene on metal surfaces.<sup>3, 12, 16, 21</sup> However, atomic hydrogen does intercalate graphene supported on SiC, but only on the condition that the sample is kept above  $\sim 723$  K,<sup>19, 20</sup> while our hydrogenation takes place at 170 K. As known that graphene is an effective gas-tight layer, vibrational modes have to be excited in the graphene layer before

hydrogen atoms are allowed to leak through and reach the interface between graphene and the substrate, but here the temperature of 170 K is too low for that. The intercalation would indeed lead to a shift of the C 1s binding energies to lower energies; however, also a shift in the  $\pi$  and  $\sigma$  band of graphene by approximately the same amount is expected (see e.g. the intercalation of gold<sup>22</sup>), which we did not observe. In order to identify a possible hydrogen intercalation, the adsorption of atomic hydrogen on clean Ni(111) surface was also investigated. In comparison to the adsorption of atomic hydrogen on graphene/Ni(111), we find no change in the valence band, i.e. in the d-states of nickel (0 ~ 2 eV) and at ~ 6 eV that would indicate the interaction of hydrogen with the nickel surface (see supporting information). This implies that hydrogen does not intercalate between graphene and Ni(111). In addition, we want to point out that the interaction of graphene with the Ni(111) substrate is very strong, such that an intercalation should not be favored, at least not at low temperatures (170 K). We can also rule out a complete conversion of graphene to graphane, since the total carbon amount influenced by hydrogen exposure levels off at ~ 1 ML, compared to the 2 ML required for a full graphane layer (see below).

To this end, it seems reasonable that hydrogen adsorbs on graphene from the top, and the C-H bonds are responsible for the new peak at 284.28 eV. The fitting procedure is illustrated for the hydrogen exposure of 90 L as an example in Fig. 1 (c). In total, four peaks are obtained; the three of them are assigned to graphene (284.96 and 284.48 eV) and nickel carbide (283.56 eV) which are not affected by hydrogen, and the fourth at 284.28 eV to the C-H structure (in red). Please note that in contrast to earlier work of Ng et al,<sup>16</sup> we do not find a contribution at a higher binding energy of ~ 285.3 eV, i.e. at a value higher than that of the original  $sp^2$  carbon signals (this is true for all of our adsorption and also dehydrogenation experiments; see Fig. 3 (a)). Furthermore, in our data the species at 284.28 eV is much more pronounced (60% of total carbon area) than observed for the saturated case in Ng's work (29 %). The lower value could be due to a different sample preparation that leads to only partially hydrogen-saturated graphene.

To compare to earlier studies and to validate our preparation method we also studied the interaction of hydrogen with graphene supported on gold/Ni(111); the corresponding data are shown in the supporting information. Due to the gold intercalation, the main carbon peak shifts to 284.33 eV. Upon exposing graphene/Au/Ni(111) to atomic hydrogen at 170 K, only one new species emerges at 284.90 eV (i.e. at higher binding energy), which is assigned to C-H bonds, with a saturation coverage of 0.45 ML (~22 %) at an exposure of 0.5 L of hydrogen.

In contrast to the case of H/graphene/Ni(111), no species is visible at lower binding energies, even after exposing graphene with up to 180 L of atomic hydrogen. Please note that the interaction between graphene and the intercalated gold layer is comparatively weak, thus intercalation of hydrogen is expected to occur here more easily. These results are in good agreement with the work of Haberer et.al,<sup>12</sup> where also very similar coverages of a C-H species were found indicating the existence of a C<sub>4</sub>H polymer-like structures. These strongly different results concerning the saturation coverage as well as in the spectroscopic signature of hydrogen on graphene indicate that the reaction between graphene and hydrogen is strongly influenced by the substrate, allowing for a tunable hydrogen storage capacity.

The TPD spectra of H/graphene/Ni(111) are shown in Fig.2 for different hydrogen exposures. The spectra of 180 and 360 L of hydrogen are similar, showing the saturation of the surface with hydrogen at these exposures (also seen in the XPS data discussed above). There are two main hydrogen desorption peaks at ~367 and ~603 K, corresponding to two hydrogen desorption states for hydrogenated graphene on Ni(111). The two shoulders at ~235 and ~314 K are attributed to the desorption of hydrogen from the back side of the nickel crystal (please refer for TPD spectra of hydrogen on Ni(111) in the supporting information). As the hydrogen exposure decreases, the peak at ~367 K declines and disappears below an exposure of 40 L. In contrast, the peak at ~ 603 K due to decomposition of the more stable C-H structures remains almost constant between 360 and 40 L and decreases at lower exposures. The broad and flat desorption region from 200 ~ 400 K is induced by hydrogen desorption from the sample holder and the back side of the nickel crystal. TPD experiments of hydrogen absorbed on a clean Ni(111) surface were used as reference to obtain the hydrogen coverage on graphene on Ni(111). For an exposure of 180 L of hydrogen, the hydrogen coverages of the two desorption peaks at 367 and 603 K are ~1.0 and ~0.2 ML, respectively.

The dehydrogenation process was also investigated with TP-XPS in order to obtain a more detailed picture of the surface processes. Fig. 3(a) shows C 1s spectra taken during dehydrogenation of graphene hydrogenated with 90 L of atomic hydrogen. As the temperature rises, the contribution at 284.28 eV decreases significantly up to 380 K and disappears completely until 650 K, where the C 1s spectrum of pristine graphene is restored. This is in line with a bond scission of the C-H structures on the surface, and desorption dihydrogen molecules from graphene surface. This shows that the hydrogenation and dehydrogenation of graphene is completely reversible, which is important for the application of graphene as hydrogen storage material. In order to visualize the dehydrogenation process in detail, the

coverage evolution of every carbon species is shown as a function of temperature in Fig. 3 (b). Note that the total amount of carbon (black markers) remains constant at  $\sim 2$  ML, implying no loss of carbon during dehydrogenation. From the signal of the C-H structures (red line), clearly a two-step dehydrogenation is evident as function of temperature. At the beginning (170 K), the coverage of the C-H species is 1.10 ML ( $\sim 59\%$ ), which is stable up to a temperature of 300 K. This contribution drops to 0.26 ML (14%) upon further heating to 400 K, indicating the first dehydrogenation step. Simultaneously, the coverage of the  $sp^2$  hybridized carbon species (green line) increase. The second dehydrogenation step is observed from 550 to 650 K, after which, the C-H species is completely decomposed, resulting in the restoration of graphene. A differentiation of the TP-XPS curve as a function of temperature (see Figure S4 in supporting information) shows the two maximum desorption peaks at 360 and 600 K, as also observed in the TPD spectra in Fig. 2. The decreases in coverage by 0.84 and 0.26 ML, respectively, in Fig. (4b) at these two temperatures, is in good agreement with the TPD data. The dehydrogenation process for a lower exposures of 0.5 L atomic hydrogen is shown in Fig. 3 (c) and (d). Interestingly, only one dehydrogenation step between 550 and 650 K is found, which is similar to the high temperature dehydrogenation step observed after 90 L hydrogen exposure. The coverage of C-H remains constant at 0.34 ML (18 %) until 550 K, and graphene is fully restored above 650 K. These results are also in line with our TPD data, which also show only a high temperature peak for low exposures.

All XPS data of different hydrogen exposures are summarized in Table S1 in the supporting information, and the corresponding curves are plotted in Fig. 4. Fig.4 (a) shows the coverage evolution of the C-H related carbon species as a function of temperature for hydrogenated graphene/Ni(111) with different hydrogen exposures, and (b) shows the coverage evolution of  $sp^2$  graphene carbon (the sum of  $sp^2$  main peak and the shoulder). For low hydrogen exposures (0.05  $\sim$  6 L), the C-H species and  $sp^2$  carbon stay almost constant, i.e. now low temperature dehydrogenation is found, when the sample is heated up from 170 to 400 K. From 550 to 650 K, the high temperature dehydrogenation step is observed, i.e., the C-H species vanishes, accompanied by the restoration of the the  $sp^2$  graphene carbon signal (to values close to 2 ML). For 0.05 L hydrogen, 0.19 ML (10 %) of C-H species is formed; this value increases to 0.35 ML (19 %) for 0.5 and 6 L hydrogen. For higher hydrogen exposures (40  $\sim$  360 L), the dehydrogenation process shows two steps at 360 and 600 K, as was also found in the TPD data. For 90 L hydrogen, the hydrogenation reaches saturation, with 1.10 ML (59 %) of C-H, as can be seen from the similar thermal evolution for 90 and 180 L hydrogen. For 360 L hydrogen, less C-H species is found at 170 K (see Figure S5 and Table

S1 in supporting information), which might be due to excess hydrogen on the surface that induces recombinative desorption of molecular hydrogen from the graphene surface.

From our TPD and TP-XPS data we can also estimate the activation energies by a simple Redhead analysis,<sup>23</sup> assuming a frequency factor  $\nu$  of  $10^{13} \text{ s}^{-1}$ . From this analysis, the activation energies of dehydrogenation for 360 K desorption is estimated to be 0.81 eV, and the one at 600 K to be 1.75 eV.

In the effort to describe the dehydrogenation processes on graphene in dependence of the substrate we also performed experiments on the dehydrogenation of hydrogenated graphene/Au/Ni(111) by TPXPS, see Figure S6 in supporting information. During the dehydrogenation process, only one desorption state starting from 470 K, with graphene being restored at 600 K is found. In comparison to the case of hydrogenated graphene/Ni(111), the temperature needed for complete dehydrogenation is lower. In addition, the maximum desorption temperature is estimated at 530 K, and the activation energy is 1.46 eV according to Redhead analysis.<sup>23</sup>

In the following, we want to shortly discuss possible structures of hydrogen on the surface. From the coverage we determined we propose the model in Fig. 5. In the cases of fully hydrogenated graphene/Ni(111) (i.e. for 90 L exposure), hydrogen atoms adsorb on every second carbon atom, yielding graphane-like  $\text{C}_2\text{H}$  structure (Fig. 5, left). The fraction of carbon atoms affected by hydrogen is 50%, in line with our XPS data (47-60 %). This  $\text{C}_2\text{H}$  structure is not very stable and thus starts to decompose at 300 K. This low temperature decomposition results in a structure where only every sixth carbon atom is bound by hydrogen, i.e., a  $\text{C}_6\text{H}$  structure. One possible arrangement is shown in (Fig. 5, center). This  $\text{C}_6\text{H}$  structure is stable up to 550 K. At temperatures higher than 650 K, all hydrogen atoms desorb and the original graphene structure is restored. The H/C ratio of  $\text{C}_6\text{H}$  structure should be 17%, in line with our data (12 ~ 20 %). In summary, the hydrogenation of graphene/Ni(111) can be described as following: upon graphene/Ni(111) is exposed to atomic hydrogen, monomers of C-H are formed, resulting in a  $\text{C}_6\text{H}$  structure for low hydrogen exposures of up to ~ 16 L. The  $\text{C}_6\text{H}$  structure is stable up to 550 K, as seen in the TPXPS and TPD data. Continuously increasing the atomic hydrogen exposure (from 40 L), leads to a second adsorption state, a  $\text{C}_2\text{H}$  structure. Since literature indicates that single-sided hydrogenation of graphene would create a material that is thermodynamically unstable,<sup>2, 24</sup> the  $\text{C}_2\text{H}$  structure is less stable compared to  $\text{C}_6\text{H}$  structure. Dehydrogenation of the partially hydrogenated graphene/Ni(111) ( $\text{C}_6\text{H}$  structure) shows one desorption state of hydrogen from 550 to 650 K, with the rate

maximum at 600 K. In contrast, dehydrogenation of fully hydrogenated graphene/Ni(111) ( $C_2H$  structure) shows two desorption states. In the first step, 2/3 of hydrogen is desorbed with the rate maximum at 360 K, transforming into the  $C_6H$  structure. The second dehydrogenation step is the same as in the case of partially hydrogenated graphene ( $C_6H$  structure).

## **Conclusion**

We studied the hydrogenation of graphene supported on Ni(111) and the corresponding dehydrogenation process by XPS and TPD. Our results indicate that a  $C_6H$  structure forms at low hydrogen exposures, and a  $C_2H$  structure forms as the second stable hydrogenation state at higher hydrogen exposures. During the dehydrogenation process, first the  $C_2H$  structure decomposes under hydrogen release and transforms into the  $C_6H$  structure at temperatures between 300 and 400 K. Subsequently, the  $C_6H$  structure decomposes starting at 550 K, and is completely dehydrogenated at 650 K, resulting in restored graphene. The activation energies for dehydrogenation are derived as 0.74 and 1.75 eV for the two successive dehydrogenation steps.

## **Acknowledgement:**

The authors gratefully acknowledge the funding of the German Research Council (DFG) by the Collaborative Research Center 953 and by the Cluster of Excellence “Engineering of Advanced Materials” ([www.eam.uni-erlangen.de](http://www.eam.uni-erlangen.de)) at the University of Erlangen-Nuremberg. W. Zhao thanks the China Scholarship Council for financing his Ph.D grant. We thank BESSY staff for their support during beamtime and the HZB for the allocation of synchrotron beamtime.

## Figures

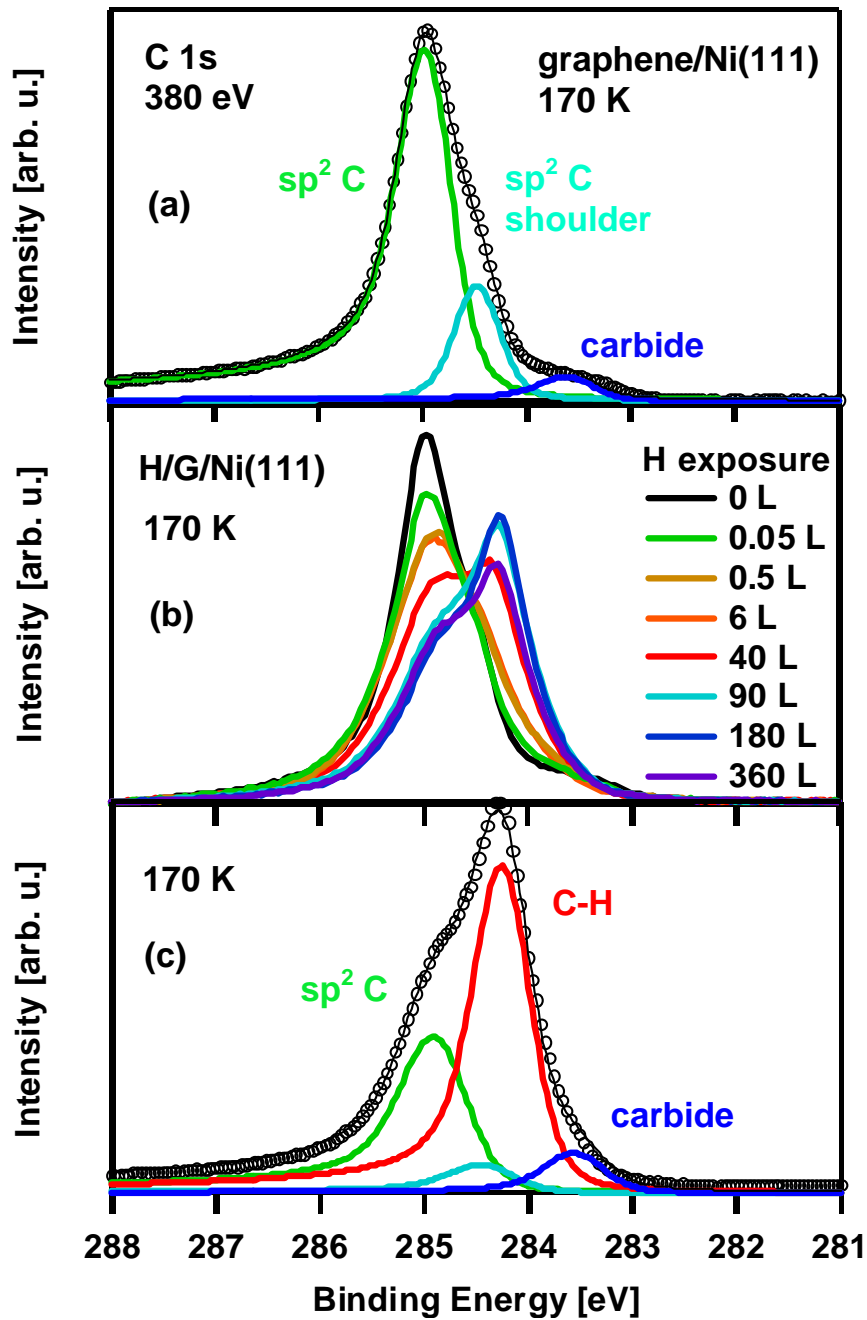


**Figure 1:** (a) C 1s spectrum of pristine graphene on Ni(111) at 170 K along with the deconvolution into different contributions: green curve ( $sp^2$  C), light blue curve ( $sp^2$  C shoulder), and dark blue curve (carbide). (b) Evolution of C 1s region upon hydrogenation of graphene/Ni(111) as a function of hydrogen exposure (0 - 360 L), measured at 170 K. (c) Deconvolution of C 1s spectrum of hydrogenated graphene/Ni(111) at 90 L H. The comparison to the C 1s spectrum of pristine graphene in (a) shows one new species, which is assigned to C-H bonds (in red).

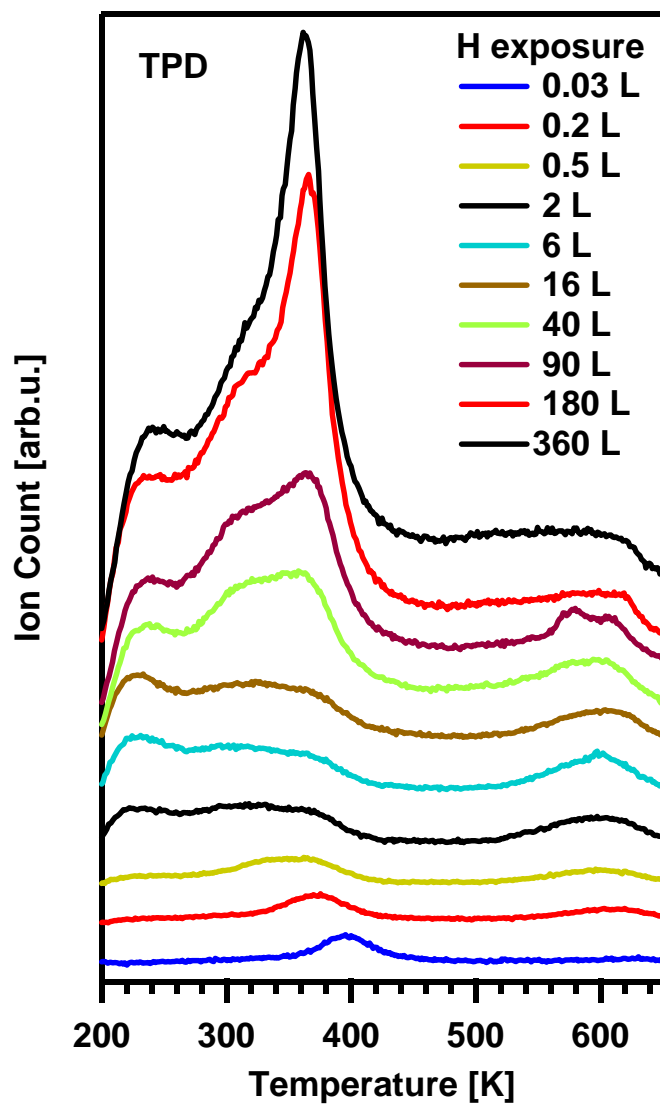


**Figure 2:** Temperature-programmed desorption (TPD) spectra as a function of hydrogen exposure (0.03 ~ 360 L); heating rate = 3 K/s; measured  $m/e = 2$ .

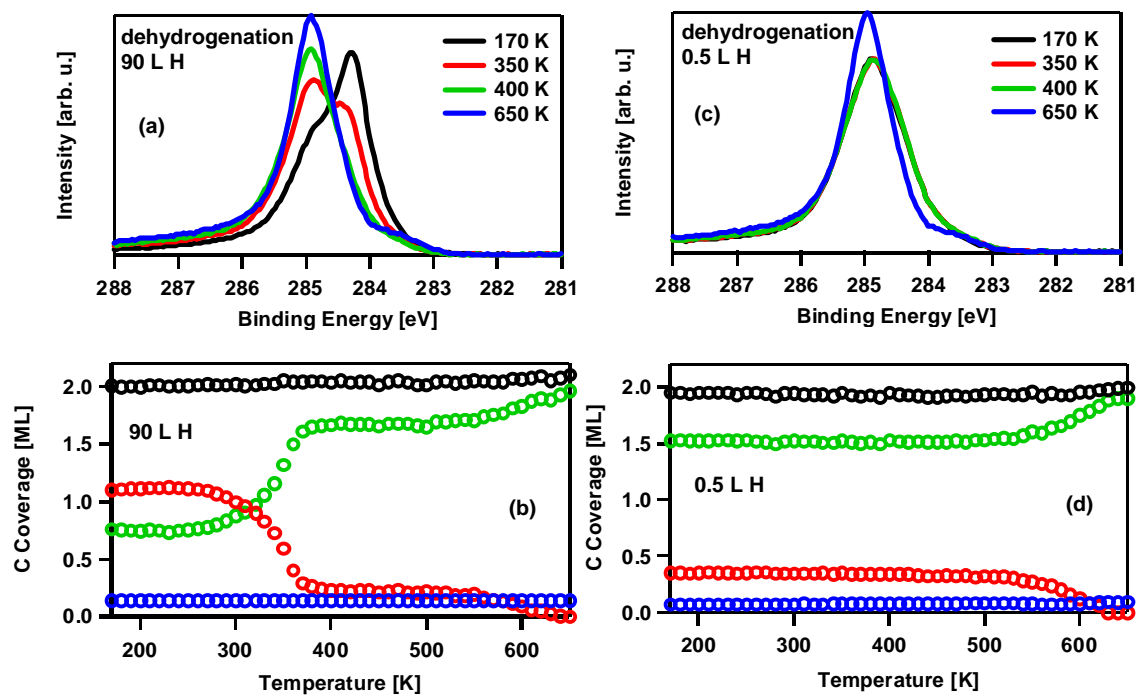


**Figure 3:** (a) and (c): Evolution of the C 1s region of hydrogenated graphene/Ni(111) with 90 L and 0.5 L hydrogen during temperature-programmed heating to 650 K; heating rate = 0.5 K/s. (b) and (d): corresponding coverages evolution of the different species as a function of temperature,  $sp^3$  C-H carbon (in red),  $sp^2$  graphene carbon (in green), carbide (in blue), total carbon (in black).

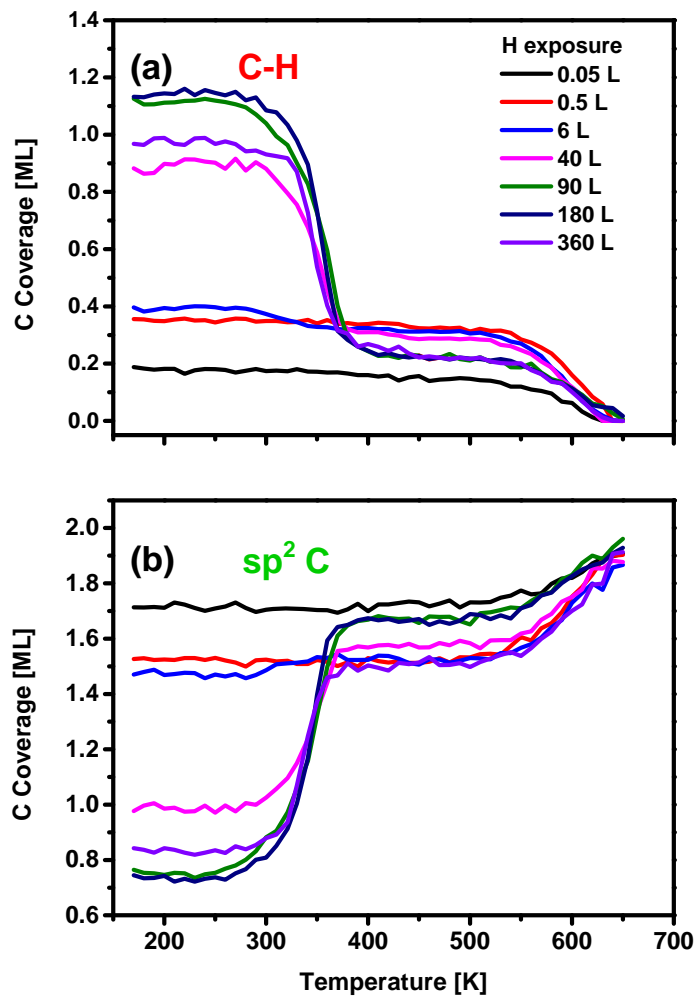


**Figure 4:** Thermal evolution of the coverage of (a)  $sp^3$  C-H carbon and (b)  $sp^2$  graphene carbon for hydrogenated graphene/Ni(111), obtained by exposure to increasing amounts of atomic hydrogen. Heating rate: 0.5 K/s.

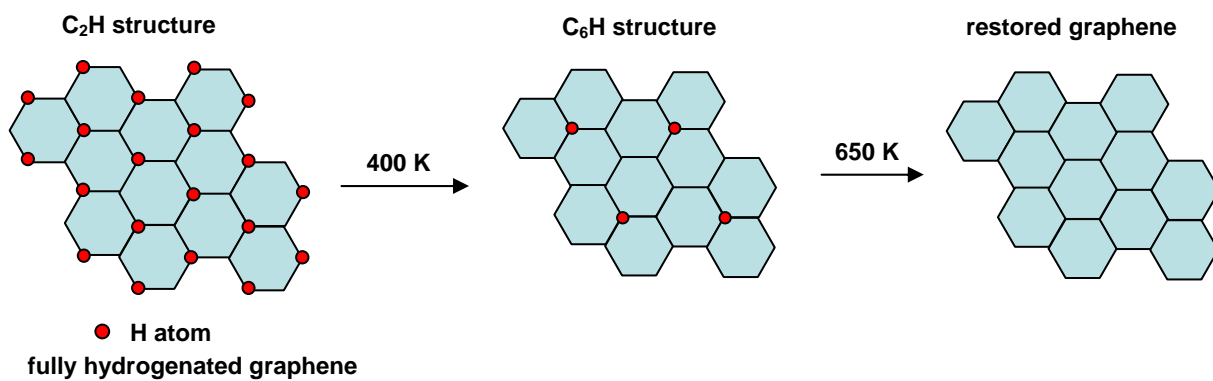


**Figure 5:** Schematic model of the dehydrogenation process of fully hydrogenated graphene/Ni(111).

## References

- (1) Tozzini, V.; Pellegrini, V. Prospects for Hydrogen Storage in Graphene. *Phys. Chem. Chem. Phys.* **2013**, *15*, 80-89.
- (2) Sofo, J.O.; Chaudhari, A.S.; Barber, G.D. Graphane: A Two-Dimensional Hydrocarbon. *Phys. Rev. B* **2007**, *75*, 153401.
- (3) Elias, D.C.; Nair, R.R.; Mohiuddin, T.M.G.; Morozov, S.V.; Blake, P.; Halsall, M.P.; Ferrari, A.C.; Boukhvalov, D.W.; Katsnelson, M.I.; Geim, A.K., *et al.* Control of Graphene's Properties by Reversible Hydrogenation: Evidence for Graphane. *Science* **2009**, *323*, 610-613.
- (4) Novoselov, K.S.; Geim, A.K.; Morozov, S.V.; Jiang, D.; Zhang, Y.; Dubonos, S.V.; Grigorieva, I.V.; Firsov, A.A. Electric Field Effect in Atomically Thin Carbon Films. *Science* **2004**, *306*, 666-669.
- (5) Castro Neto, A.H.; Guinea, F.; Peres, N.M.R.; Novoselov, K.S.; Geim, A.K. The Electronic Properties of Graphene. *Rev. Mod. Phys.* **2009**, *81*, 109-162.
- (6) Liu, H.; Liu, Y.; Zhu, D. Chemical Doping of Graphene. *J. Mater. Chem.* **2011**, *21*, 3335-3345.
- (7) Fowler, J.D.; Allen, M.J.; Tung, V.C.; Yang, Y.; Kaner, R.B.; Weiller, B.H. Practical Chemical Sensors from Chemically Derived Graphene. *ACS Nano* **2009**, *3*, 301-306.
- (8) Dan, Y.; Lu, Y.; Kybert, N.J.; Luo, Z.; Johnson, A.T.C. Intrinsic Response of Graphene Vapor Sensors. *Nano Lett.* **2009**, *9*, 1472-1475.
- (9) Bostwick, A.; McChesney, J.L.; Emtsev, K.V.; Seyller, T.; Horn, K.; Kevan, S.D.; Rotenberg, E. Quasiparticle Transformation During a Metal-Insulator Transition in Graphene. *Phys. Rev. Lett.* **2009**, *103*, 056404.
- (10) Flores, M.Z.S.; Autreto, P.A.S.; Legoas, S.B.; Galvao, D.S. Graphene to Graphane: A Theoretical Study. *Nanotechnology* **2009**, *20*, 465704.
- (11) Balog, R.; Jorgensen, B.; Nilsson, L.; Andersen, M.; Rienks, E.; Bianchi, M.; Fanetti, M.; Laegsgaard, E.; Baraldi, A.; Lizzit, S., *et al.* Bandgap Opening in Graphene Induced by Patterned Hydrogen Adsorption. *Nature Mater. Lett.* **2010**, *9*, 315-319.
- (12) Haberer, D.; Giusca, C.E.; Wang, Y.; Sachdev, H.; Fedorov, A.V.; Farjam, M.; Jafari, S.A.; Vyalikh, D.V.; Usachov, D.; Liu, X., *et al.* Evidence for a New Two-Dimensional C<sub>4</sub>h-Type Polymer Based on Hydrogenated Graphene. *Adv. Mater.* **2011**, *23*, 4497-4503.
- (13) Balog, R.; Jørgensen, B.; Wells, J.; Lægsgaard, E.; Hofmann, P.; Besenbacher, F.; Hornekær, L. Atomic Hydrogen Adsorbate Structures on Graphene. *J. Am. Chem. Soc.* **2009**, *131*, 8744-8745.
- (14) Zecho, T.; Guttler, A.; Sha, X.; Jackson, B.; Kupperts, J. Adsorption of Hydrogen and Deuterium Atoms on the (0001) Graphite Surface. *J. Chem. Phys.* **2002**, *117*, 8486-8492.
- (15) Nikitin, A.; Näslund, L.-Å.; Zhang, Z.; Nilsson, A. C-H Bond Formation at the Graphite Surface Studied with Core Level Spectroscopy. *Surf. Sci.* **2008**, *602*, 2575-2580.
- (16) Ng, M.L.; Balog, R.; Hornekær, L.; Preobrajenski, A.B.; Vinogradov, N.A.; Mårtensson, N.; Schulte, K. Controlling Hydrogenation of Graphene on Transition Metals. *J. Phys. Chem. C* **2010**, *114*, 18559-18565.
- (17) Zhao, W.; Kozlov, S.M.; Höfert, O.; Gotterbarm, K.; Lorenz, M.P.A.; Viñes, F.; Papp, C.; Görling, A.; Steinrück, H.-P. Graphene on Ni(111): Coexistence of Different Surface Structures. *J. Phys. Chem. Lett.* **2011**, *2*, 759-764.
- (18) Papp, C.; Fuhrmann, T.; Trankenschuh, B.; Denecke, R.; Steinrück, H.-P. Site Selectivity of Benzene Adsorption on Ni(111) Studied by High-Resolution X-Ray Photoelectron Spectroscopy. *Phys. Rev. B* **2006**, *73*, 235426

- (19) Virojanadara, C.; Zakharov, A.A.; Yakimova, R.; Johansson, L.I. Buffer Layer Free Large Area Bi-Layer Graphene on Sic(0001). *Surf. Sci.* **2010**, *604*, L4-L7.
- (20) Watcharinyanon, S.; Virojanadara, C.; Osiecki, J.R.; Zakharov, A.A.; Yakimova, R.; Uhrberg, R.I.G.; Johansson, L.I. Hydrogen Intercalation of Graphene Grown on 6h-Sic(0001). *Surf. Sci.* **2011**, *605*, 1662-1668.
- (21) Bunch, J.S.; Verbridge, S.S.; Alden, J.S.; van der Zande, A.M.; Parpia, J.M.; Craighead, H.G.; McEuen, P.L. Impermeable Atomic Membranes from Graphene Sheets. *Nano Lett.* **2008**, *8*, 2458-2462.
- (22) Varykhalov, A.; Sánchez-Barriga, J.; Shikin, A.M.; Biswas, C.; Vescovo, E.; Rybkin, A.; Marchenko, D.; Rader, O. Electronic and Magnetic Properties of Quasifreestanding Graphene on Ni. *Phys. Rev. Lett.* **2008**, *101*, 157601.
- (23) Redhead, P.A. Thermal Desorption of Gases. *Vacuum* **1962**, *12*, 203-211.
- (24) Boukhvalov, D.W.; Katsnelson, M.I.; Lichtenstein, A.I. Hydrogen on Graphene: Electronic Structure, Total Energy, Structural Distortions and Magnetism from First-Principles Calculations. *Phys. Rev. B* **2008**, *77*, 035427.

Supporting information for

## **Investigation of the hydrogenation and dehydrogenation of graphene / Ni(111)**

W. Zhao, F. Späth, K. Gotterbarm, C. Gleichweit, H.-P. Steinrück and C. Papp

*Lehrstuhl für Physikalische Chemie II, Universität Erlangen-Nürnberg, Egerlandstr. 3, 91058 Erlangen*

### **The influence of hydrogen adsorption to the valence band of Ni(111) and graphene/Ni(111)**

Figure S1 (a) shows valence band of clean Ni(111) and atomic hydrogen absorbed on Ni(111) after exposure of 180 L hydrogen at 170 K. In the region from 0 to 2 eV, the two resolved peaks transform into one broad peak upon hydrogen adsorption. In contrast, this feature is kept after hydrogen adsorption on graphene/Ni(111), shown in S1 (b). Moreover, the nickel satellite peak at  $\sim 6$  eV,<sup>1</sup> is shifted to higher binding energy by  $\sim 0.54$  eV due to hydrogen adsorption on Ni(111), but remains unchanged in the case of H/graphene/Ni(111). In addition, the graphene  $\pi$  band at  $\sim 9.5$  eV vanishes after hydrogenation, due to the transformation of  $sp^2$  to  $sp^3$  hybridization. Above all, it is concluded that hydrogen absorbs on the graphene surface instead of intercalation between graphene and Ni(111) upon exposing atomic hydrogen to sample.

### **XPS data of H/graphene/2 ML Au/Ni(111)**

Figure S2 (a) shows C 1s XP spectra of hydrogenated graphene supported on 2 ML Au/Ni(111) for different hydrogen exposures (0.5 - 180 L). S2 (b) shows the fit of C 1s spectrum of hydrogenated graphene/Au/Ni(111) at 40 L H. For detailed discussion see the manuscript.

### **TPD data of H/Ni(111)**

Figure S3 shows the TPD spectra of hydrogen absorbed on clean Ni(111). The saturated hydrogen on Ni(111) after exposure to 360 L atomic hydrogen shows a broad desorption region ranging from 200 to 400 K.

### **Differentiation curve of the coverage evolution of C-H species in the TPXPS data**

Figure S4 shows the differentiation curve of the coverage evolution of the C-H species in the TPXPS experiment for 90 L hydrogenated graphene/Ni(111); two “desorption” peaks are situated at 360 and 600 K, consistent with the TPD data.

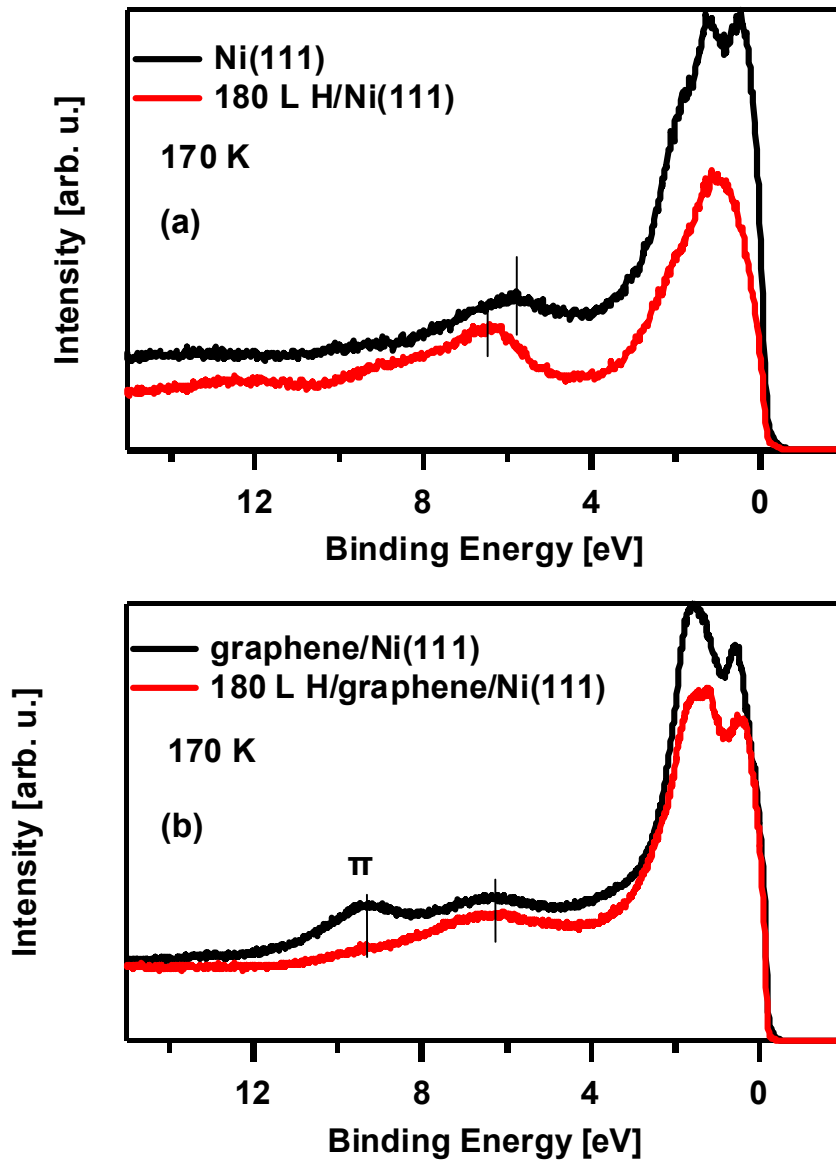
### **Coverage ratios evolution as a function of hydrogen exposures**

Figure S5 shows the evolution of the coverage ratio between sp<sup>3</sup> C-H carbon and sp<sup>2</sup> graphene carbon as a function of hydrogen exposures at 170 K. The graph shows that hydrogenated carbon (C-H) increases from 0.5 until 90 L hydrogen, where the hydrogenation reaches saturation. For 360 L hydrogen, the C-H species shows a small decrease, probably due to excess atomic hydrogen inducing recombinative desorption of molecular hydrogen from the graphene surface.

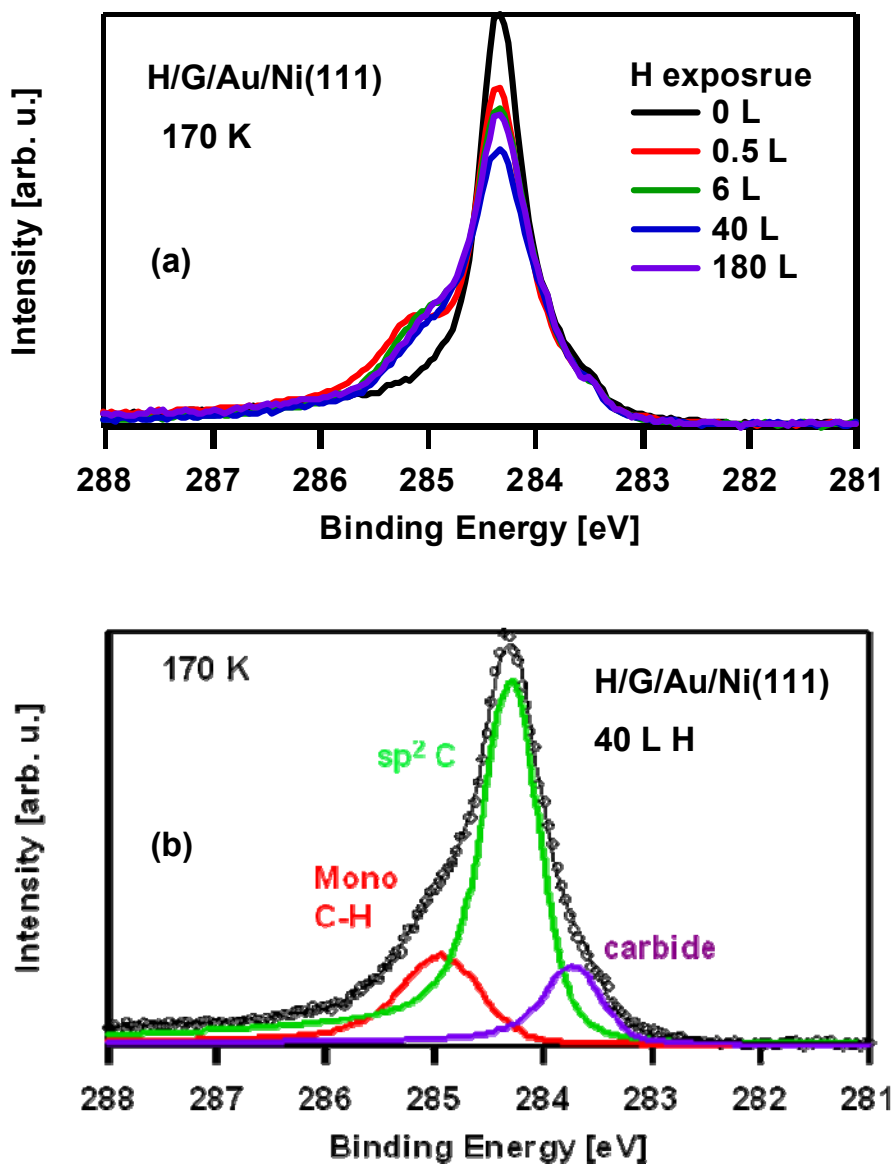
### **TPXPS data of dehydrogenation of H/Graphene/Au/Ni(111)**

Figure S6 (a) shows the evolution of C 1s region of 40 L hydrogenated graphene/Au/Ni(111) as a function of temperature. S6 (b) shows the coverage evolution of every carbon species, indicating that dehydrogenation starts at 470 K and finishes until 600 K. In comparison to the case of H/graphene/Ni(111), complete dehydrogenation occurs at a lower temperature.

Supplementary figures and captions



**Figure S1:** (a) Valence band of clean Ni(111) (black) and Ni(111) after exposure to 180 L atomic hydrogen (red). (b) Valence band of single layer graphene on Ni(111) (black) and after exposing this layer to 180 L atomic hydrogen (red). The spectra were measured at 170 K, at normal emission, and at a photon energy of 100 eV.



**Figure S2:** (a) The evolution of C 1s region of graphene/Au/Ni(111) as a function of hydrogen exposure (0 - 180 L), measured at 170 K. (b) Deconvolution of C 1s spectrum of hydrogenated graphene/Au/Ni(111) after exposure to 40 L H. the red curve at 284.90 eV corresponds to the sp<sup>3</sup> C-H,carbons, the green at 284.33 eV to sp<sup>2</sup> graphene carbon and and the purple curve at 283.70 eV to nickel carbide.

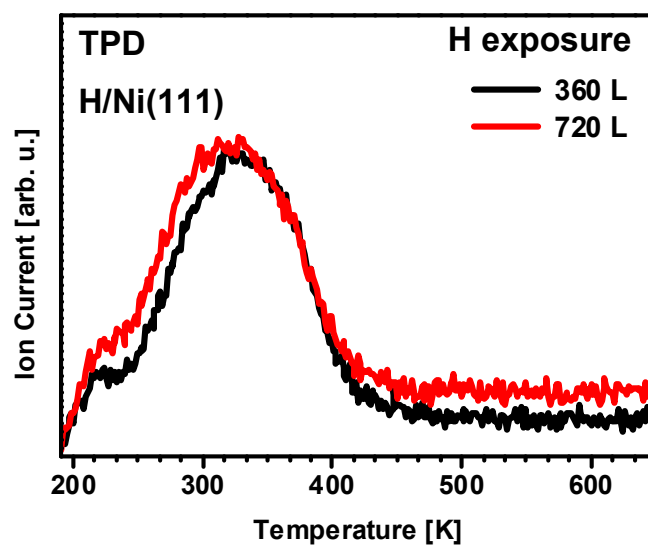


**Figure S3:** Temperature-programmed desorption (TPD) spectra of hydrogen absorbed on clean Ni(111) surface at 170 K for hydrogen exposures of 360 and 720 L); heating rate = 3 K/s; measured  $m/e = 2$ .

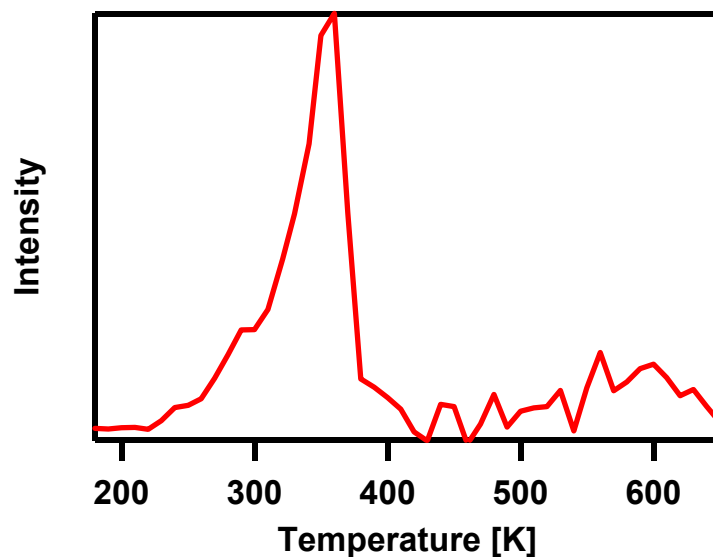


**Figure S4:** Differentiation curve of the coverage evolution of the C-H species in the TPXPS experiment after exposure of graphene/Ni(111) to 90 L atomic hydrogen.

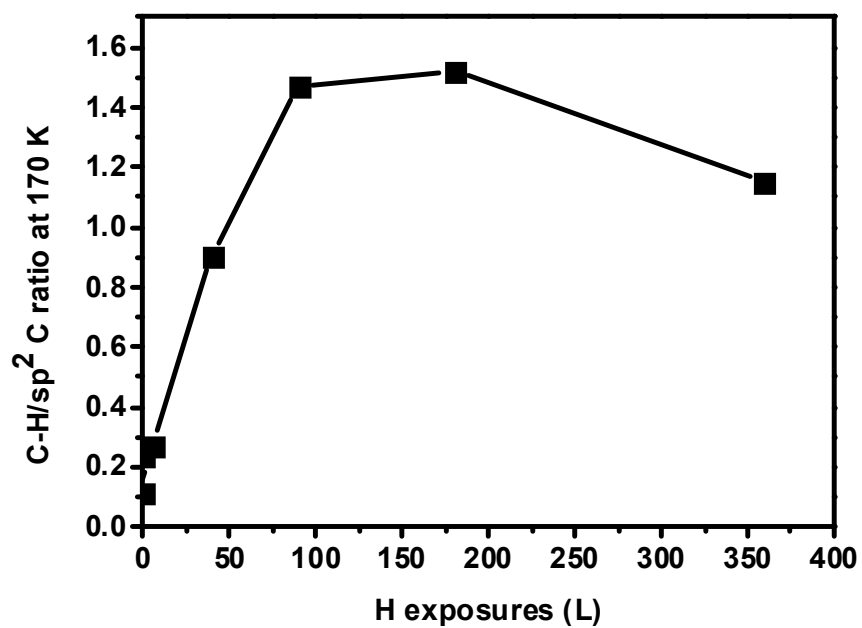


**Figure S5:** Evolution of the coverage ratios between sp<sup>3</sup> C-H carbon and sp<sup>2</sup> graphene carbon as a function of hydrogen exposure, measured at 170 K.

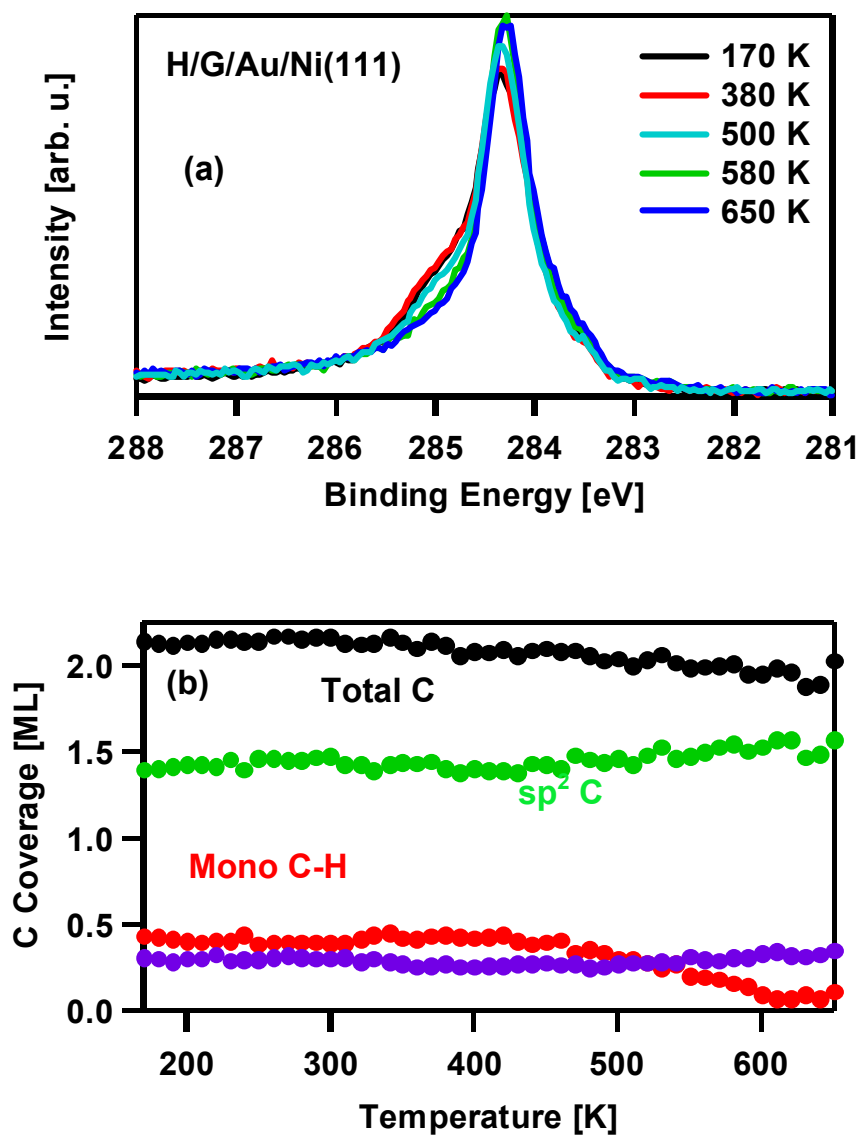


**Figure S6:** (a) Evolution of the C 1s region of 40 L hydrogenated graphene/Au/Ni(111) during TPXPS; the heating rate was 0.5 K/s. (b) Coverage evolution of the different contributions as a function of temperature:  $sp^3$  C-H carbon (red),  $sp^2$  graphene carbon (green) and nickel carbide (purple) and total carbon coverage (black).

**Table S1:** Summary of XPS data for hydrogenation of graphene/Ni(111) and for the corresponding TPXPS experiments; after different hydrogen exposures. For detailed discussion please refer to the manuscript.

H Exposure (L)	C-H(170K) (ML)	C-H(400K) (ML)	sp <sup>2</sup> C main (170 K)(ML)	Carbide (ML)	C-H at% (170 K)	C-H at% (400K)
0.05	0.19	0.17	1.72	0.09	10%	9%
0.5	0.35	0.34	1.53	0.09	19%	18%
6	0.39	0.32	1.47	0.13	21%	17%
40	0.88	0.31	0.98	0.09	47%	17%
90	1.10	0.28	0.77	0.13	59%	15%
180	1.10	0.27	0.75	0.12	59%	15%
360	0.97	0.25	0.84	0.1	54%	14%

## References

- (1) Sakisaka, Y.; Komeda, T.; Onchi, M.; Kato, H.; Masuda, S.; Yagi, K. Photoemission Study of the Valence-Band Satellite of Ni(110). *Phys. Rev. B* **1987**, *36*, 6383-6389.